Department of Physics and Astronomy
University of Heidelberg

Bachelor Thesis in Physics
submitted by

Daniel Kreuzberger

born in Rottweil (Germany)

2020

An Experimental Study on Electron-Impact Ionization of Benzene Molecules

This Bachelor Thesis has been carried out by Daniel Kreuzberger at the
Max-Planck-Institut für Kernphysik, Heidelberg
under the supervision of
Priv.-Doz. Dr. Alexander Dorn

Abstract

The aim of this work is to experimentally determine the ratio between double and single ionization of benzene in electron-molecule-collisions. Two different reaction microscopes with different geometrical properties were used for this property. The ratio was measured in an energy range of $50-1000eV$ and compared with newly published data. At the same time, the ratio between double and single ionization was measured for argon, as more well-founded data offers better comparison options. The behavior of the ratio over energy curves could be explained with the help of the Born approximation and agrees with the literature data. The absolute values, however, do not agree with the values in the literature, which could be partially explained by the properties of the reaction microscopes.

Zusammenfassung

Das Ziel dieser Arbeit ist es, das Verhältnis zwischen Doppel- und Einfachionisation von Benzol in Elektron-Molekül-Stoßreaktionen experimentell zu bestimmen. Dazu wurden zwei verschiedene Reaktionsmikroskope mit unterschiedlichen geometrischen Eigenschaften verwendet. Das Verhältnis wurde in einem Energiebereich von $50-1000eV$ gemessen und mit neu publizierten Daten verglichen. Parallel dazu wurde das Verhältnis zwischen Doppel- und Einfachionisation für Argon gemessen, da hier eine fundiertere Datenlage bessere Vergleichsmöglichkeiten bietet. Der Verlauf der Energie-Verhältnis-Kurven konnte mit Hilfe der Bornschen Näherung erklärt werden und stimmt mit den Literaturdaten überein. Die Absoluten Werte stimmen hingegen nicht mit den Werten der Literatur überein, was durch die Eigenschaften der Reaktionsmikroskope teilweise erklärt werden konnte.

Contents

Chapter 1

Theoretical Introduction

In this chapter, a short theoretical introduction on the Benzene-molecule and electron-impact ionization is given. For this, the concept of cross-sections is introduced and some of the different ionization channels are described. Afterwards a short quantum-mechanical introduction on the electron-atom collisions, including the Born approximation is given. In the end, the process of dissociation is described, which is important for understanding the measured spectra.

1.1 Benzene

Benzene is the simplest aromatic compound and is made out of six carbon and six hydrogen atoms (C_6H_6). It has an atomic mass of $m = 78.11 \frac{g}{mol}$. The carbon atoms form a hexagon with a bond angle of $\theta = 120°$ and a bond length of $139.7 pm$, which lies in between the length of a single bond ($154 pm$) and the one of a double bond ($134 pm$) [LKK16]. This is due to the overlap of the p-orbitals of the carbon atoms, which causes a continuous electron cloud above and below the carbon level (see also figure 1.1). Such a system is also called a π-system. Under normal conditions, benzene is a colorless liquid with a high refractive index. The melting point is at $6°C$ and the boiling point at $80°C$. It is produced by thermal cracking of n-hexane and is normally used as an additional component of fossil fuels. In the past, it was widely used as a solvent, but, due to its toxic and especially carcinogenic properties, it was replaced by other substances.

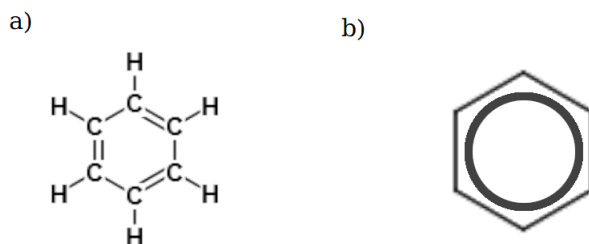When gaseous benzene gets emitted in a vacuum at very low temperatures,

Figure 1.1:   a) Skeletal formula of benzene, b) Widely used symbol for benzene, which underlines the π-system.

like for example in a supersonic jet expansion, clusters of benzene-rings are forming due to the Van-der-Waals forces. One can see molecules of the form $(C_6H_6)_n$ with n going up to 40 [AKi+88].

1.2   Ionization with electrons

The ionization with electrons is described by a wide field of different processes. The common ground of them is that an electron interacts with the target and at least one electron of the target is emitted into the continuum. In the context of this work, two processes are of special interest:

$$A + e^- \rightarrow A^+ + 2e^- \tag{1.1}$$

$$A + e^- \rightarrow A^{++} + 3e^- \tag{1.2}$$

Equation 1.1 on the one hand describes the single ionization process, while equation 1.2 on the other hand describes the double ionization.
The electron impact single ionization is one of the most common processes in particle physics and has therefore already been investigated for several decades. First experimental uses of the ionization with electrons are reported in the 1910 years (i.e. [Dem16]). Shortly after this, first attempts were made to describe this process in the context of quantum mechanics. This led, amongst other theories, to the Born-Approximation, which will be discussed later and was published in 1926 [Bor26]. With this approximation, one was able to theoretically describe both the single and the double ionization. In the recent past, more and more researchers use the crossed beam

technique, where the target and the electron beam are crossed in a small area to investigate the ionization behavior for various atoms and molecules to get an insight in the quantum mechanics of more complex systems.

One can of course also link the experimental results to the quantum-mechanical theories. The method of choice is here the concept of ionization cross-sections. The (double) differential cross-section $\frac{d^3\sigma_i}{dE_i d\Omega}$ for each ionization channel is defined by the following relation:

$$N_i = \frac{d^3\sigma_i(E_0, E_i, \Omega)}{dE_i d\Omega} N_e N_t \qquad (1.3)$$

In this equation N_i is the ion gain in the direction $d\Omega$ and with the energy $E_i + dE_i$, N_e the electron beam (unit: $particles/(a.u.)^2 s$) and N_t the target density. The energy E_0 is the energy of the projectile [MW95].

From those differential cross-sections one can calculate the total ionization cross-section (TICS). To obtain this, one has to sum over all involved reaction channels i and integrate over all directions and final state energies:

$$\sigma_I(E_0) = \sum_i \int \int \frac{d^3\sigma_i(E_0, E_i, \Omega)}{dE_i d\Omega} d\Omega dE_i \qquad (1.4)$$

This TICS is given in units of $area^2$ and has typical values of several $\mathring{A}^2$ for the single ionization of benzene [Sin+16]. When we now want to connect this TICS, which can be measured in experiments, to the quantum mechanical theory, we find the simple relation

$$\sigma_I \propto |T_{fi}|^2 \,, \qquad (1.5)$$

where T_{fi} is the calculated transition amplitude.

After this short introduction on the method of cross sections, we can have a closer look on some of the individual ionization channels. A more detailed description of the following ionization concepts can also be found in [Dür06] and [Pfl].

1.2.1   Single ionization

The most common ionization process is the single ionization. There just one electron gets emitted into the continuum and the ion is left in the ground

state. We see a reaction of the type

$$A + e^- \rightarrow A^+ + 2e^- \ . \tag{1.6}$$

This is just a general expression, the actual process of course depends on multiple values like the ionization energy and the ionization cross-section. This cross-section is heavily dependent on the electron energy and will be evaluated in the measurements (see also chapter 3). Another important factor is the kinematic of the atom-electron-collision: The distance and the velocity of the electron relative to the atom matters.

Since the diameter of an atom is small compared to the mean distance between the atoms in the target beam, the most likely case is an interaction where the distance between the target and the projectile is large. In this case, there is only a small momentum transfer and the momentum of the ion is more or less the same after the ionization. This process is described by the exchange of one virtual photon. Therefore, the ionization characteristic is very similar to the photo-ionization (see figure 1.2).
The other extreme case is of course a direct collision between the projectile electron and the target electron which is emitted into the continuum. In that type of reaction, a big amount of the projectile momentum is transferred to the target electron. The momentum of the ion stays the same, similar to the other extreme case. Due to the direct momentum transfer, the electron is preferentially emitted in the direction of the transferred momentum $\vec{q}$. This can be seen in figure 1.2. One can also see a smaller maximum in the opposite direction of $\vec{q}$. To emit an electron in this direction, it has to be scattered in the coulomb potential of the ion. In this case a lot of the momentum $\vec{q}$ is transferred to the ion.

One last case to consider is the ionization near the threshold, if the projectile has only slightly more energy than the ionization threshold. This kinematic region is extremely difficult for theoretical calculations, since the two slow continuum electrons are strongly correlated and they are both moving in the field of the ion for a long time. This is described by the so called Wannier theory, which can be studied in detail in [Wan53], but a small introduction can also be found in [MW95]. The most important result of this theory in the context of this work is the so called Wannier threshold law:

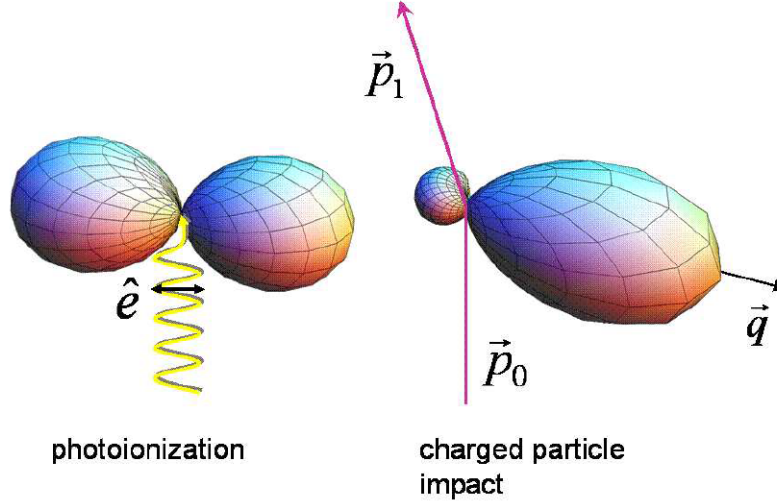$$\sigma_I \propto E^n \ . \tag{1.7}$$

Figure 1.2: Differential cross-sections - On the left side: Cross-section for the photo-ionization as an analogy for the electron-induced ionization at wide distances, on the right side for the charged particle impact, like the direct electron-electron collision. The distance from the surface to the coordinate origin is the value of the differential cross-section $d\sigma^2/d\Omega$. Data is calculated at an arbitrary electron energy well above the ionization threshold (from [Dür06]).

The exponent n depends on the charge of the ion Z:

$$n = \frac{1}{4}\left[\left(\frac{100Z-9}{4Z-1}\right)^{1/2} - 1\right].$$

(1.8)

In this work, ions of the charge $Z = 1$ and $Z = 2$ will appear. This leads to values of $n = 1.127$ and $n = 1.056$.

1.2.2   Double Ionization

The more complex process is the double ionization. Here not only a single interaction occurs, but also a second interaction has to take place in the reaction process to release a second electron. This can be reached by various reaction channels.
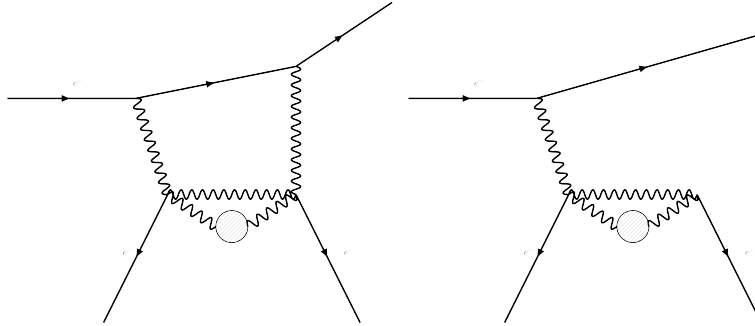
Figure 1.3: Schematic drawings of double ionization processes: On the left side a TS2 process, where the projectile interacts with both emitted electrons, on the right side a TS1 process, where the projectile only interacts with one electron and the second one is emitted by interatomic or intermolecular process.

The most intuitive process is the direct reaction channel, where the projectile first interacts with one electron and afterwards with the second, while both target electrons are emitted into the continuum. This interaction is done via the exchange of two virtual photons, so the characteristic of this process is very similar to the two photon double ionization. This process is of second order, because the projectile interacts two times. Due to this double interaction, one calls this process a Two-step process (TS2). A schematic representation of this process can be seen in figure 1.3 on the left side.

A somehow very similar process is the TS1 mechanism: The 1 indicates a first order process, so the projectile interacts only once with the electron. In contrast to the single ionization, a second electron is emitted by an internal process of the form:

$$A^+ + e^- \rightarrow A^{++} + 2e^- \tag{1.9}$$

This is also done via the exchange of a virtual photon (see also figure 1.3, now the photon represents both the electron-electron interaction like in the TS2 process and the exchange of a virtual photon).

The third possible process is the shakeoff-mechanism (SO). There, the fist electron is directly ejected and the second electron is ejected due to the change of the ion potential: If the first electron is not there anymore, the shielding of the potential is changed and therefore it can happen that the

wave-function of the second electron is not a eigenfunction of the changed effective potential. If this is the case, the electron can be emitted into the continuum under certain conditions. But of course other processes can occur that don't lead to ionization, like the emission of a photon.

The total double-ionization cross-section is then, like in equation 1.4, the sum over the cross-sections of each reaction channel:

$$\sigma^{++} = \sigma_{TS2} + \sigma_{TS1} + \sigma_{SO} \tag{1.10}$$

1.3   The Born approximation

As mentioned previously, the ionization cross-section is directly proportional to the absolute squared of the quantum mechanical transition amplitude (see 1.5). So to get a theoretical prediction of the measured cross section, one has to calculate this transition amplitude.
The problem of this calculation is, that even for the simplest of all ionization problems, the single ionization of hydrogen, an analytical solution does not exist. Therefore one has to do some complex numerical calculations or introduce some approximations. A good overview of many different methods is given in the book [MW95].

The Born approximation is one of those approximate methods. In this approximation, the system is divided into a independent target- and a projectile system. The only interaction of those systems is during the time of the collision, before and afterwards they are not effecting each other. Because of the $1/r$ shape of the coulomb potentials, this is obviously not true in real situations. The following presentation of the Born approximation is following the lines from [Pfl]. Assume we have an initial and a final state of the shape

$$|\phi\rangle = (2\pi)^{-3/2} e^{ip_p R} |\varphi\rangle , \tag{1.11}$$

while the projectile of the momentum p_p at the position R is described by a plane wave and the target electron state is $|\varphi\rangle$. The Hamilton-operator of the system is given by

$$\hat{H} = \hat{H}_0 + \hat{V} = \hat{H}_{Proj} + \hat{H}_{Tar} + \hat{V} , \tag{1.12}$$

where $\hat{H}_{Proj}$ is the Hamiltonian of the free projectile, $\hat{H}_{Tar}$ the Hamiltonian of the free target and $\hat{V}$ is the interaction of of both the projectile and the target. One finds the relation

$$\hat{V} = \frac{Z_p Z_t}{R} - \sum_j \frac{Z_p}{|R - r_j|} \; . \tag{1.13}$$

Here Z_p and Z_t are the charges of the projectile respectively of the target. The target-core is in the coordinate origin and r_j is the position of the target electron j. So with this we can set up the Schrödinger-equation for this system:

$$(E - \hat{H}_0)|\phi\rangle = \hat{V}|\phi\rangle \; . \tag{1.14}$$

Another important point of the Born approximation is the solution of this Schrödinger-equation. It is solved with the so called Lippmann-Schwinger equation, which gives an iterative solution for the transition amplitude T_{fi}:

$$T_{fi} = \langle\phi_f|T|\phi_i\rangle = \langle\phi_f|\hat{V} + \hat{V}\hat{G}_0^+\hat{V} + \hat{V}\hat{G}_0^+\hat{V}\hat{G}_0^+\hat{V} + ...|\phi_i\rangle \; . \tag{1.15}$$

The operator $\hat{G}_0^+$ is the Greens operator, which describes the propagation of the system between two interactions. This is intuitively clear, since the potential $\hat{V}$ describes the actual interaction. So the iteration done in equation 1.15 is an iteration over the orders of the process: The first term describes a first order process with just one interaction, the second one a second order process with two interactions and the propagation between the iterations and so on. So this series is an expansion in powers of the interaction potential $\hat{V}$. It only converges if the interaction potential is weak, which can be reached if the projectile is very fast, so that the interaction time is short. Therefore the Born-Approximation is not valid for ionization with low projectile energies. In the so called "first Born approximation", one only uses the first term of the series for the calculation of the amplitude, in the "second Born approximation" one also use the second term. Higher order terms are normally not used for calculations, since for this one would need very high mathematical effort.

1.3.1   First Born approximation

As mentioned before, the first Born approximation is the first order term of equation 1.15:

$$T_{fi}^{1B} = \langle\phi_f|\hat{V}|\phi_i\rangle \; . \tag{1.16}$$

We can now insert the interaction potential 1.13 as well as the equation for the system 1.11, and get

$$T_{fi}^{1B} = \frac{Z_p}{2\pi^2 q^2} \langle \varphi_f | \sum_j e^{iqr_j} | \varphi_i \rangle = \alpha_1 Z_p \,. \tag{1.17}$$

For the actual calculation of the transition amplitude T_{fi}^{1B} it is necessary to calculate the wave functions of the bound states $|\varphi_i\rangle$ and continuum states $|\varphi_f\rangle$ of the target. This is of course not trivial for an atom with more than one electron or even a molecule. For simplification one uses a hydrogen-like model, with one electron only and an effective nuclear charge Z_t' instead.

1.3.2   Second Born approximation

If one wants to also make a calculation for the double ionization, one has to use the second Born approximation, since at least two interactions are necessary for this process. The second Born approximation also uses the second order term of the equation 1.15:

$$T_{fi}^{2B} = \langle \phi_f | \hat{V} \hat{G}_0^+ \hat{V} | \phi_i \rangle \,. \tag{1.18}$$

The actual calculation of T_{fi}^{2B} is of course even more complex than the one of T_{fi}^{1B}. But since the Greens operator is:

$$\hat{G}_0^+ = \lim_{\epsilon \to 0} \frac{1}{E - \hat{H}_0 + i\epsilon} \,, \tag{1.19}$$

one can simplify equation 1.18 similarly to equation 1.17:

$$T_{fi}^{2B} = \alpha_2 Z_p^2 \,. \tag{1.20}$$

Of course we do not gain any information on α_2 with this simplification. This factor is still the result of complex calculations which would go beyond the scope of this work. But with equation 1.20 we can set up a nice equation for the cross-section calculated with the second Born approximation:

$$\sigma_{2B} \propto |T_{fi}^{1B} + T_{fi}^{2B}|^2 = \alpha_1^2 Z_p^2 + 2\alpha_1 \alpha_2 Z_p^3 + \alpha_2^2 Z_p^4 \,. \tag{1.21}$$
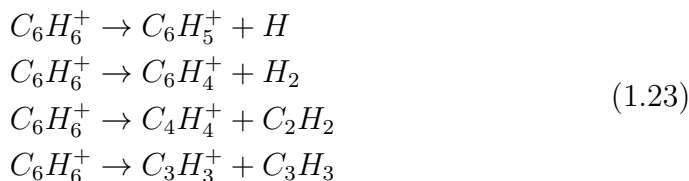
Here one can once more clearly distinguish between the one step ionization, which is related to the first term and the two step ionization, which is related to the last term. The middle term $2\alpha_1\alpha_2 Z_p^3$ is related to an interference of both processes.

1.4   Electron impact dissociation

Kitau and Nakatsuji stated that the ground state of benzene is [KN87]:

$$...(3e_{1u})^4(1a_{2u})^2(3e_{2g})^4(1e_{1g})^4 \ . \tag{1.22}$$

If one or two electrons from the $(1e_{1g})$ orbital are released, the resulting ion is in the ground state. In processes like this, the stable Bz^+ or Bz^{++} ions are produced. At sufficiently high electron energies, it is possible that an electron from a lower orbital is released. If this happens, an excited ion is produced. Due to intramolecular processes, this electronic excitation is converted to a vibrational excitation of the electron ground state. If the excitation energy is higher than the dissociation-threshold, the molecule breaks up and one can see the fragments in the experiment [Tal+00]. Due to the complexity of benzene, there are many different dissociation channels, which are accessible at different threshold energies. An excellent overview on all processes is given in [Hol+02]. One can see that the threshold energies of all dissociation processes are around $15-25eV$ so they should be accessible in our experiment. Of course some of the dissociation channels are more likely and other are less likely, which is why some of the fragment ions can not be seen due to the statistical background. The four most prominent reaction channels are:

$$\begin{aligned}
C_6H_6^+ &\rightarrow C_6H_5^+ + H \\
C_6H_6^+ &\rightarrow C_6H_4^+ + H_2 \\
C_6H_6^+ &\rightarrow C_4H_4^+ + C_2H_2 \\
C_6H_6^+ &\rightarrow C_3H_3^+ + C_3H_3
\end{aligned} \tag{1.23}$$

In the experiment, the neutral fragments can not be detected, but the charged ions can be seen in the Time of flight (TOF) -spectra . A typical measurement can be seen in figure 1.4. This dissociation plays an important role in the correction of the background and in the comparison of the ionization cross-section to the total cross-section.
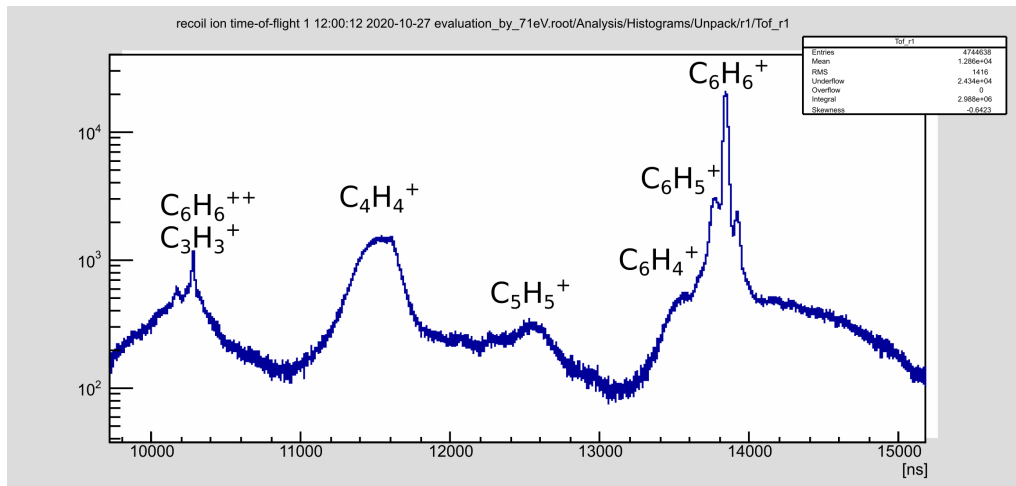
Figure 1.4: TOF-spectrum of an ionization measurement of benzene. The electron energy was $E_e = 71eV$. Some fragments can be clearly determined. Since the TOF only depends on the ration q/m, the time is the same for $C_3H_3^+$ and $C_6H_6^{++}$. Due to the dissociation-duration, the $C_3H_3^+$ peak is broadened and the $C_6H_6^{++}$ peak is a sharp peak on top.

Chapter 2

Experimental Setup

In this chapter, the general set up of the firstly used reaction microscope is described. Also a further description of some special experimental techniques like the super-sonic gas jet generation and the creation of a well defined electron beam is given. The probably most important thing in the reaction microscope, the time and position sensitive ion detector is described. Then a short explanation of the data acquisition, digitalization and processing is given. In the end, the differences of the second reaction microscope which was used in later measurements, were described.

2.1 Setup of the reaction microscope

The whole experiment is placed in a big vacuum chamber (more on that in section 2.1.2). Inside this vacuum chamber, there are various areas for different purposes. On top of the chamber, there is the gas jet creation system, in which the supersonic gas jet is created. On the bottom is the so called gas dump, two chambers where the unused part of the gas jet is pumped away to keep the reaction chamber clean. Between those areas is the main chamber. It is formed like a tube. On both sides of this tube are detectors. On one side, there is an electron detector, which will not be used in the context of this work and on the other side, there is the ion detector. In front of the Ion detector, there is a pulsed electron gun, which points towards the middle of the electron detector. This gun sends a pulsed electron beam, which crosses the gas jet in the reaction area, so there can be reaction processes between the gas jet and the electrons. Electrons which

do not react with the jet pass the electron detector in a small tube in the middle of the detector area and get caught behind the detector.

2.1.1 The spectrometer

For the detection of the particles, it is necessary to accelerate them towards the detectors. Otherwise, for example ions with a velocity in the direction of the electron detector can not be detected. This well defined acceleration is also necessary to record the momentum of the particles. Since electrons are negative and ions are positive charged particles, this acceleration is done with a electric field. This has the advantage that the electrons are guided to the electron detector and the ions to the ion detector just because of the sign of their charges. The electric field is produced by ring-shaped copper plates, which are aligned parallel and connected via resistors (see also figure A.4 and A.5). In this arrangement, the plates act as voltage dividers and produce a homogeneous field in the middle. This field is aligned parallel to the electron beam. Therefore, electrons which do not react just pass the main chamber straightly. The problem for more general experiments with the need for detection of the electrons is, that the velocity of the electrons is much higher than the one of ions due to the lower mass of the electrons. Therefore the resolution of the momentum caused only by the electric field is not good enough. To avoid this problem, there is a pair of Helmholtz coils around the experiment, which produces a homogeneous magnetic field parallel to the electron beam. So the electrons produced or deflected in the reaction volume are not flying parallel to the field any more and therefore moving on a spiral track. This increases the time of flight of the electrons. Since the acceleration of particles with the mass m, the charge q and the momentum $\vec{p}$ in the magnetic field $\vec{B}$ is:

$$\vec{a} = \frac{q}{m^2} \vec{p} \times \vec{B} \tag{2.1}$$

and the mass of an ion is $10^3 - 10^4$ times higher than the one of an electron, the acceleration on an ion is negligible.

2.1.2 The vacuum system

The vacuum system of the experiment is rather complex: There are three forepumps (rotary vane pumps) to get the whole chamber to a basic pressure
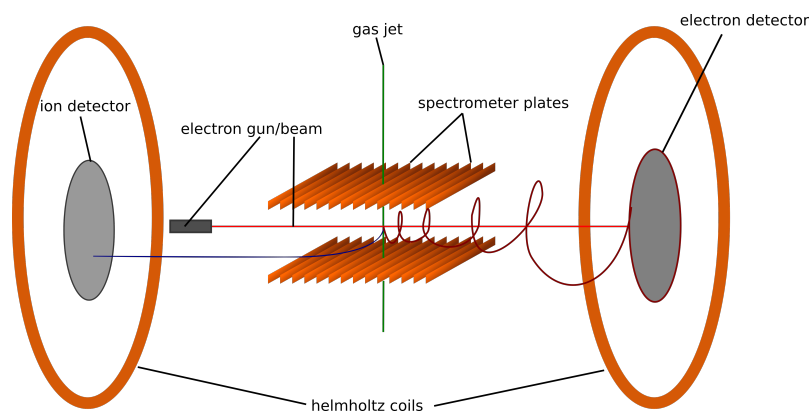
Figure 2.1: Schematic drawing of the spectrometer (spectrometer plates are square shaped for better visualisation).

of $10^{-3} mbar$. Once this pressure is reached, overall eight turbomolecular pumps are used to get to the working pressure(see figure 2.2). The aim of this system is to get a very low pressure in the main chamber, so in the ideal case, there are no other particles than the ones from the gas jet. Molecules/atoms that are not from the gas jet of course also get ionized, but mostly not in the dedicated reaction volume of the experiment and therefore can be seen in the detector as a continuous background (see also figure 3.1). Another aim of the vacuum system is to create a high pressure difference between the gas reservoir and the jet chamber one, because this is necessary for a good jet quality. More on that in the next chapter.

2.2   Target beam - supersonic gas expansion

When one prepares the target, one thing to think about is the momentum of the particles before the reaction. The easiest way to investigate a reaction is to have the target in rest and a projectile with a well defined momentum. This is of course not practicable in an experiment, since we want to investigate many reactions to get an overview over the statistics of the reaction. A second way is to have a target with a well defined, directed and small momentum. Especially the thermal energy of the target has to be small compared to the energy of the target after the reaction. This is what we get in a supersonic gas expansion [Sch+97].
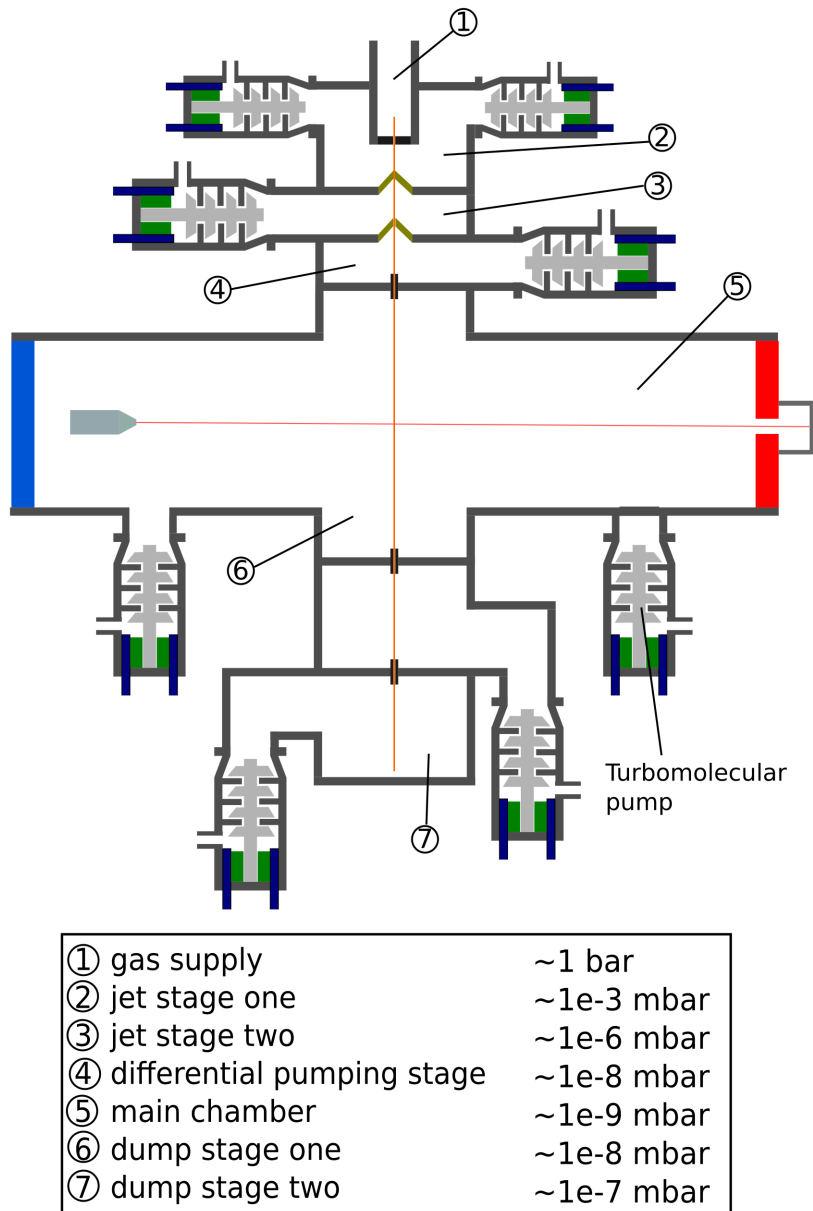
Figure 2.2: Schematic drawing of the vacuum system of the experiment(Without forepumps) and the typical working pressures.

In principle, supersonic gas expansion happens when a gas flows from a reser-

voir at high pressure through a small nozzle in an area of low pressure. The entropy is conserved in this process. Because the volume density decreases, the momentum space density has to increase, what is equivalent to a decrease of temperature. To quantize this process, we have to look at the free enthalpy H, which is the sum of the thermal energy and the energy induced by the gas pressure:

$$H = E_{therm} + E_{press} \; . \tag{2.2}$$

From the Maxwell distribution we get $E_{therm} = \frac{3}{2}kT_0$ and from simple kinetic gas theory of ideal gases $E_{press} = kT_0$ where k is Boltzmann's constant and T_0 is the temperature of the gas reservoir. So we have:

$$H = \frac{5}{2}kT_0 \; . \tag{2.3}$$

In the ideal supersonic gas expansion, this free enthalpy is totally converted into kinetic energy, so we get after the expansion:

$$v_{jet} = \sqrt{\frac{5kT_0}{M}} \; , \tag{2.4}$$

with the atomic mass of the gas M and:

$$T = \frac{2}{3k}E_{therm} = 0K \; . \tag{2.5}$$

Now we look at this gas expansion in a more detailed way. For this, we consider a one dimensional model (see also chapter 2.2 in [Fis00]). As before, the gas in the reservoir is at temperature T_0 and has the pressure p_0. In addition, the number density of the molecules is n_0 and the velocity is $v_0 \neq 0$. The gas in this reservoir can expand in x-direction through the nozzle into an area with low pressure p_1. All the parameters of the gas (pressure p, number density n, temperature T, velocity v and cross section area of the beam A) only depends on x, not on y and z. One also assumes once more to have an ideal gas, so one can use the ideal gas law $p = nkT$. In addition one uses the adiabatic equation $dn/n = (3/5)dp/p$. Since no gas can escape the system, the number of particles is conserved ($d(nAv) = 0$). If one combines Newton's law ($(dv/dt)Mn = -dp/dx$) with the ideal gas law, one can find:

$$\frac{dp}{p} = -v\frac{M}{kT}dv \; . \tag{2.6}$$

One can also combine the adiabatic equation with the conservation of the number of particles and get:

$$\frac{dp}{p} = -\frac{5}{3}\left(\frac{dA}{A} + \frac{dv}{v}\right) . \tag{2.7}$$

From equation 2.6 and equation 2.7 we get:

$$\frac{dA}{A} = \left(\left(\frac{v^2}{s^2}\right) - 1\right)\frac{dv}{v} , \tag{2.8}$$

with the local sound velocity $s = \sqrt{5kT/3M}$ (M is the mass of a gas particle). Since the nozzle is very small (typically $\sim 30\mu m$) the gasjet has to converge towards it. Therefore $dA > 0$ and with 2.8 one gets that $dv > 0$ for $v < s$. This means that the molecules get accelerated. With a reasonable ratio $p_0/p_1 >> 1$ the molecules can reach the local sound velocity, but they can not accelerate further, since then $v > s$ and therefore $dv < 0$. So at the nozzle all the gas molecules have the local sound velocity $v_n = s = \sqrt{5kT/3M}$. The index n marks that the parameters have this value at the nozzle.

Beyond the nozzle, the cross section area of the beam increases, so $dA > 0$. But to make a prediction on dv with equation 2.8 one has to consider that the local sound velocity s also changes because of the dependence on the temperature T. By inserting the ideal gas law into the adiabatic equation, one finds the following expression:

$$\frac{dp}{p} = \frac{5}{2}\frac{dT}{T} . \tag{2.9}$$

One can again insert this into the equation 2.6:

$$dT = -\frac{5}{2}\frac{M}{k}vdv \tag{2.10}$$

This equation can easily be integrated:

$$T = T_n - \frac{M}{5k}v^2 \tag{2.11}$$

This can now be inserted in the expression for the local speed of sound:

$$s^2 = \frac{5k}{3M}\left(T_n - \frac{M}{5k}v^2\right) = s_n^2 - \frac{v^2}{3} . \tag{2.12}$$

One can now use once more the equation 2.8:

$$\frac{dA}{A} = \left(\left(\frac{v^2}{s_n^2 - \frac{v^2}{3}}\right) - 1\right)\frac{dv}{v} = \left(\left(\frac{x}{1 - \frac{x^2}{3}}\right) - \frac{1}{x}\right) dx .$$ (2.13)

In the second step one introduces the simple substitution: $x \equiv v/s_n$ Now one can integrate the whole expression to get the cross section area of the beam behind the nozzle. From the assumption that the beam is at the local speed of sound at the nozzle, one gets the lower integration limit $x_n = v_n/s_n = \sqrt{3/2}$:

$$\int_{A_n}^{A} \frac{dA}{A} = \int_{x_n}^{x} \left(\frac{x}{1 - x^2/3} - \frac{1}{x}\right) dx .$$ (2.14)

This leads to the result:

$$\frac{A}{A_n} = \frac{9}{16x\left(1 - \frac{x^2}{3}\right)^{3/2}} .$$ (2.15)

When one looks at a point far behind the nozzle, the ratio $\frac{A}{A_n}$ gets very large. Therefore the denominator of equation 2.15 has to get small. One can find that $x \to \sqrt{3}$. When one now resubstitutes x, one gets the value of the velocity of the jet beam:

$$v_{jet} = \sqrt{3}s_n = \sqrt{\frac{5kT_n}{M}} .$$ (2.16)

One can easily see that this velocity is higher than the local sound velocity at the nozzle, so this is why this technique is called "supersonic gas expansion". On the other hand, one can see that this value perfectly agrees with the one given from the contemplation of the free enthalpy in equation 2.4. As one has seen before, the temperature of the gas jet is 0 at this velocity. But this velocity is only reached for the simplification $\frac{A}{A_n} = \infty$. This will be of course never reached. So the real temperature is (with 2.11 2.15):

$$\frac{T}{T_n} = \left(\frac{3\sqrt{3}}{16}\frac{A_n}{A}\right) .$$ (2.17)

This equation is only usable for theoretical considerations, since A/A_n can not be measured in an easy way. Therefore one has introduced the speedratio S:

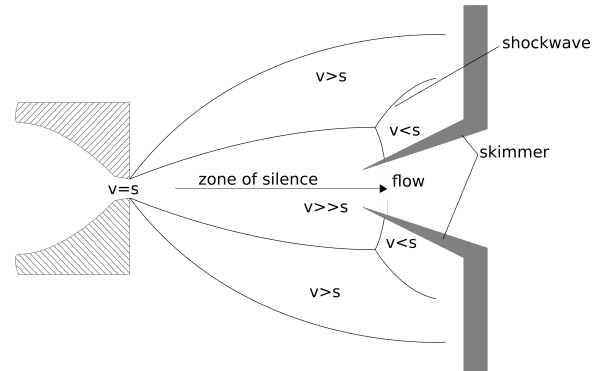$$S = \frac{v_{jet}}{v_{therm}} = \sqrt{\frac{5T_0}{2T}} .$$ (2.18)

Figure 2.3: shockwaves and zone of silence in the supersonic gas expansion (from [DRM88], modified).

Typical values for this speedratio are $10 < S < 100$. Those values can be reached with low technical effort even with higher diameters of the nozzle. The limiting factor is the power of the pumps at the expansion chamber [HKE03].

Another interesting thing to look at is the distribution of different velocity zones in the expansion chamber. Since there is no absolute vacuum in this chamber, the molecules of the jet can collide to other particles and loose some of their velocity. At some point the beam is so much slowed down that the particles move with a velocity slower than the speed of sound. In this part of the jet, pressure waves (i.e. from reflections at the chambers walls) can move freely in the beam, especially against the direction of the beam. But when such a wave reaches the supersonic part of the beam, it can not go further against the beam, because every pressure wave can only move at the speed of sound. Therefore, a shockfront is formed at the border of the supersonic zone (also called "zone of silence"). This is of course highly undesirable, because pressure, temperature, density and velocity are fluctuating heavily in those shockfronts. One has to keep in mind that the main advantage of the supersonic gas expansion is the well defined velocity and direction of the particle beam. Therefore, in the experiment a skimmer is used to separate a small beam out of the zone of silence and cut away all the other parts of the beam (see figure 2.3).

As seen in figure 2.2, there are two other chambers between the expansion

chamber and the main chamber. Those chambers belong to a differential pumping system: In the expansion chamber, a skimmer with a relatively wide aperture of ⌀ $= 200\mu m$ is used. So the jet remaining is also relatively tall. This has the advantage, that not all of the gas has to be pumped away by the first two turbomolecular pumps and that the pressure in the expansion chamber is not too big. In the second chamber, a skimmer with the aperture of ⌀ $= 400\mu m$ is used to form the beam into its final shape [Pfl12]. After this skimmer, all particles fly in the same direction without collision. In the third chamber, a small tube is used to connect it to the main chamber. This tube acts like a blockade for particles which are not in the beam and it reduces the pressure difference between the main chamber and the last skimmer. On the opposite side of the main chamber, another tube leads to the first jet dump stage, where a part of the jet gets pumped away, while the remaining part gets through a second tube in the second dump stage. There the gas is totally pumped away.

2.3   The electron beam

The electron beam is produced in an electron gun, which is placed in front of the ion detector (see figure 2.1). For the measurement of the time of flight, it is necessary to have a well defined, short electron pulse. This makes the construction of such an electron gun very difficult, since, in addition it should be quite small, so it won't shade the detector that much. In the experiment, an ultraviolet laser is used to solve this problem: This laser can be easily pulsed even with small pulse lengths of several $0.1ns$. The intensity can be varied by an variable density filter in the optical path. For the sake of convenience, both, the filter and the laser are placed outside the vacuum chamber. The light beam enters the vacuum chamber through a small window and hits a tantalum photocathode. The electrons are released from this photocathode due to the photo-electrical effect. The laser has a wavelength of $622nm$ [Ren+14], so the energy of the photons can be easily calculated:

$$E_{ph} = \frac{hc}{\lambda} = 4,66eV \tag{2.19}$$

Tantalum has the electron affinity of $E_{ea} = 4,19eV$ [Jüsar]. So the electrons have the following kinetic energy, when they are released:

$$E_{kin} < E_{ph} - E_{ae} = 0,47eV \tag{2.20}$$

This is also the uncertainty of the energy in the beam, since all the electrons are afterwards accelerated to the necessary energy in the same electrical field. Since this energy is normally in the range of $\sim 100eV$, the relative uncertainty is very small. After the electrons have been accelerated, they are focused by four electrostatic lenses, so they hit the target beam in the optimal way. Behind the collision area, the electrons which have not collided to any target particles pass the electron detector through a small hole in the middle and get caught in the electron dump. Another thing to mention is that the size of the electron gun is only $8mm$ in diameter and $60mm$ in the length, so it does not shade much area on the ion detector.

2.4   The Ion detector

One essential part of the experiment is the position sensitive detection of the ions produced during the collision. Position sensitivity is very important for the determination of the masses and the charges of the ions, from which we can determine the kind of ions. Another thing we want to measure with the ion detector is the time of flight of the ions, which is typically very short. So the detector has to have a small reaction time. Another very fundamental problem is that one single ion can not be detected because the signal to noise ratio is too high. Therefore the charge of the ion has to be amplified in the detector before processing it further. To solve the tasks and problems, there are two different elements combined in the detector: First the ions hit a *microchannel plate* (MCP, see section 2.4.1), then the signal is processed by a position sensitive anode, the so called *delayline anode* (see section 2.4.2).

2.4.1   Microchannel plate

A MCP is in principle a position sensitive amplifier for particles: On the front side a charged particle or a high energetic photon, here those particles are ions, hits the plate and on the backside a cloud of electrons is released. To reach this functionality, the structure of the MCP is simple but difficult to produce:

The MCP is basically a plate of glas, with millions of small, parallel channels of diameter $10 - 100\mu m$. The electron clouds are produced only in those channels, so the resolution of the position is limited due to the size of the

channels

incident
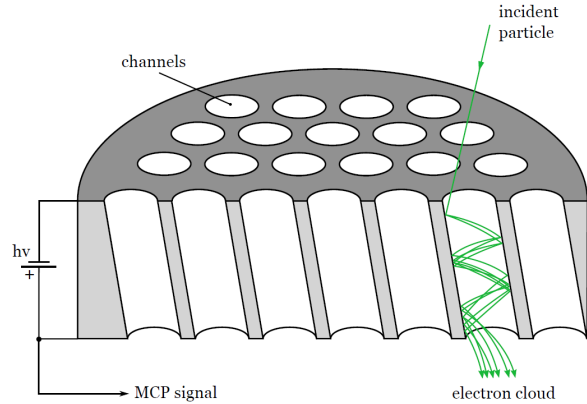particle

hv

MCP signal

electron cloud

Figure 2.4: Schematic drawing of a MCP and its working principle, from [Pfl12].

walls between the channels. For the production of those electrons, a high voltage potential is applied between the front side and the back side of the MCP. To provide a homogeneous field all over the plate, both sides are coated with a metal surface of low resistance. Therefore the potential is position independent. The walls of the channels are coated with a layer of a semiconductor material (e.g. GaP, $GaAsP$). This layer has a high resistance, but a small work function for electrons. As soon as a particle hits the wall of a channel, several electrons get kicked out the wall and get accelerated in the potential between front and back. Then they hit the wall again and more electrons get released. So a chain reaction takes place in the channel and the electron cloud is released at the back of the MCP. This electron cloud can now be further processed with the delayline anode. With commercially available MCPs, amplifications of 10^4 can be reached. The death time is normally smaller than $1ns$ [Wiz79].

The information of the time of the impact (important for the TOF) is gained by looking at the HV-signal of the MCP. Since lots of electrons get released by an impact, the voltage goes up for about $10ns$. This pulse can be coupled out via a capacitor and amplified for further analysis.

To produce such a MCP, techniques from fiber optics production are applied. First, one glass tube filled with another glass, which is soluble in chemical

etchant. This tube is now drawn to a small diameter. Then many of such drawn tubes are packed in a hexagonal multi-fibers. Those are drawn again and packed in a glass envelope. This product is now sliced and the slices are beveled and polished. Afterwards the soluble cores are etched away to get the channels. Finally, the surfaces (metallic and semiconductor material) are vapor-deposited.

One problem of the MCP is the so called *positive ion feedback*: due to the high electron energies in the electron cloud, the remaining background gas can be ionized or ions from the channel walls can be released. Without any prevention, those ions get accelerated in the HV-field of the MCP and then released in the main chamber of the reaction microscope. In the field of the reaction microscope, they get accelerated to the opposite direction and can then hit the MCP again, creating a void signal. To prevent this, the channels are tilted against the MCP (as implied in figure 2.4), so the ions hit the wall of the channels after a short time. Therefore the energy is too low to create new free electrons. If one wants to get a higher amplification, one can also mount multiple MCPs after each other. Then one can use the so called *chevron configuration*, where the angle of the channels differs from plate to plate. This prevents the positive ion feedback in an effective way.

2.4.2   Delayline Hexanode

For the position sensitive detection of the electron clouds released on the MCP, one needs a special anode, the so called delayline anode. This anode made out of several insulated wires which are placed in a special way (see figure 2.5a)). Two wires are placed parallel to each other and they are placed in multiple parallel rows to cover the area of the detector. Another wire arrangement is placed on this, but turned around by 90°. So there is a grid of wires on the MCP. In each layer of this grid, one wire is positively biased and one is neutral. Therefore, an incoming electron cloud will be split up on the positively biased wires ("signal wires"). The difference between this signal and the one from the parallel wire ("reference wire") can now be amplified with an differential amplifier (DA). Since background and noise is mostly the same for both wires, it is neglected in the difference and the signal to noise ratio gets significantly better. One now wants a position sensitivity detection of the electron cloud, so one has to look at the running time in the wire. When such an electron cloud is absorbed by the wire, the charge splits
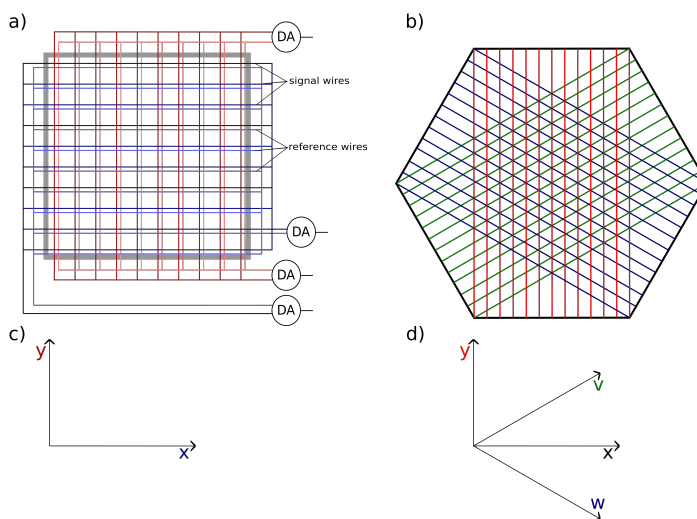
Figure 2.5:   a) schematic drawing of a conventional delayline anode with signal wires and reference wires, b) schematic drawing of the used hexagonal delayline anode, c) coordinate system of the conventional anode, d) coordinate system of the hexanode.

up and both parts run with a constant velocity v_{wire} to the opposite ends of the cables. Therefore one can now evaluate the time difference between the signals and can assume the origin of the charge.

The signal of the MCP at the time t_0 is the starting point of the charge, since the time of flight of the electrons between the MCP and the anode is negligible. So this signal starts two timers, which are stopped by the signals of the DAs. This results the times t_1 and t_2. With those times one can easily calculate the position of the origin of the charge relative to the center of the wire:

$$x = v_{wire}((t_1 - t_0) - (t_2 - t_0)) = v_{wire}(t_1 - t_2) . \qquad (2.21)$$

The second, turned layer is read out in the same way and therefore produces the second coordinate y. One practical thing about this delayline anodes is that the time sum for each layer:

$$t_{sum} = (t_1 - t_0) + (t_2 - t_0) = const. \qquad (2.22)$$

is obviously constant. Therefore, this can be used as a condition in the signal

processing: only if both layers have the same, pre-defined t_{sum}, the event is used as a 'good' event.

Another practical thing is, that even if one of the time signals of the anode is lost, the position of the impact can be calculated from the remaining time t_{rem}. The missing time t_{mis} is simply:

$$t_{mis} = t_{sum} - t_{rem} + 2t_0 \ . \tag{2.23}$$

But what if, due to multiple impacts, both, one time signal and the starting signal is lost? This can happen in both coordinate direction: x and y and in both cases the signal is lost. To prevent this from happening, a hexanode is used in the experiment. The special thing about the hexanode is that there is a third layer of wires, which means a third coordinate used to have a redundancy. The three layers have now an angle of 60°, so they have a hexagonal structure (see fig. 2.5b)). So for the Cartesian coordinates we have to do a transformation (can be seen in [Dür06], schematic in fig. 2.5d)), but we can lose the starting signal as well as one time signal and have enough data to get the position of the impact.

2.5   Data acquisition and processing

All the signals from the experiment have to be converted into digital information for the processing and evaluation. This is done with various electrical components: The pulse of the MCP is first amplified and then converted with a *constant fraction discriminator* (CFD). This CFD is an instrument which creates a standard-pulse when a certain threshold is exceeded. As mentioned before, the signals from the delayline hexanode are amplified with DAs to minimize the noise of the signals. All the signals, from the MCP and the DAs are evaluated in a *time to digital converter* (TDC). In addition, the pulse of the laser is also used in this TDC to have the ability of calculating the TOF of the ions. The TDC can calculate the time difference between this starting pulse and the other signals. All those differences are then converted into digital signals. A VME-bus system transports this signals to the VME-front-end computer, on which they get stored.

For the further processing of the data, the program *go4* is used. This program is based on the library ROOT, which was developed at the CERN. *go4* has a *graphical user interface* (GUI) where all the results are shown in a clearly structured way. It is also able to create diagrams and histograms. Another

ability of this program is to sort and evaluate the data, i.e. to sort out background events and to fit curves to the data.

2.6   New experimental setup

In the course of the measurements, a second reaction microscope was used for additional experiments (see chapter 3.6). This setup differs from the described one due to a changed geometry and other things. The spectrometer is now perpendicular to electron beam. So there is no electron gun in front of the detector. The electron gun itself is also changed: There is a constantly heated cathode, but the electron beam is periodically blocked by a pulsed field. The experiment does not have an electron detector, which is not necessary for the measurements done in the context of this work. Since the electrons of the beam fly perpendicular to the spectrometer, it is also operated by a pulsed field, which is ramped up after the electrons have hit the target beam. So the focusing on the target remains good. The target beam itself is once more produced in a super sonic gas expansion. For the evaluation, the software *CoboldPC* is used in this experiment, whose functions are roughly the same as the ones of *go4*.

Chapter 3

Measurements and Evaluation

The aim of this chapter is to present the various measurements and evaluations done in the context of this work. First an old measurement on the ionization of benzene at four different energies was evaluated. In a second step this measurement was reproduced and extended. Then some alternative measuring methods were tried to improve the results. In the end, a new experimental setup was used for another measurement on the ratio between single and double ionization of benzene and also, for testing properties, of argon.

3.1 Old measurement on double ionization of benzene

In this measurement we want to investigate the Ratio $R = \sigma^{++}/\sigma^+$ of the cross-sections for the double and single ionization. Therefore we have to localize the peaks of $C_6H_6^{++}$ and $C_6H_6^+$ in the TOF-spectra. Then we have to quantize the number of counts in both peaks. One special challenge is to separate the valid counts from the background, especially when there are other reaction-products in the same TOF-range. Since the Rate of events Z is

$$Z = \sigma \cdot n \cdot dx \cdot l \,, \tag{3.1}$$

with the ionisation cross-section σ, the target density n, the target length dx and the projectile rate l, the ratio of the cross sections is equal to the ratio of the rates of events [Pfl]. In real measurements, the actual counting rate is

Name of the setting	Value	purpose of setting
use Tsum Check Hits	on	Later hits are checked for valid time sums
Tsum Check First Hit	on	First hit is used to check for valid time sum
Tsum Check Last Hit	on	First hit is used to check for valid time sum
use TSum Check Hits Double MCP	off	Later hits are checked with doubled MCP signals
use Reco Delayline	on	Reconstructs missing delayline data
use Reco MCP	on	Reconstructs missing MCP data from the dealayline data

Table 3.1: General settings for the $g04$ analysis.

also dependent on the detector efficiency ϵ, so the rate of events measured is

$$Z = \epsilon \cdot \sigma \cdot n \cdot dx \cdot l \,. \tag{3.2}$$

The data of this measurement was taken at the reaction microscope on 08/30/2019. As only the ion-detection part is relevant for the measurement of the ionization, the electron detector was not in operation. There are four measurements at the projectile energies $41eV$, $71eV$, $151eV$ and $301eV$. So a relatively wide range of energies is covered by this data.

Data analysis

The data analysation was done with the program $go4$ and a self-made *Python*-routine. In the $go4$ analysis, there were some data reconstruction functions used. As mentioned above, one can reconstruct missing delayline and MCP-data. The setting used in the analysis was the following:

The time sum conditions are set separately for each energy, but were obviously the same for both the single and double ionization-analysis to have the same basic conditions. The data was now evaluated for each peak separately. Each peak was analyzed with five different settings to reduce the background and verify the results:

1. Without any condition, just the counts over TOF-spectra in the area of the peak.

2. With a reduction of the x-range of the detector on the area of the peak. The number of counts over the TOF is displayed in the Histogram.

3. With a reduction of the y-range of the detector on the area of the peak. The number of counts over the TOF is displayed in the Histogram.

4. With a time condition, so only the counts in the TOF-range of the peak are displayed. The y-direction limits are wide and the counts over x-position are shown the histogram

5. With the same conditions as in 4. but with a narrow y-range.

This five histograms are now imported with the *python*-routine. In this program one can set the borders of the peaks and can fit various functions in the histogram. Dependent on the shape of the data, two or three gaussian functions are used for the fit. One is for the main peak and the others for the background. To verify the use of gaussian functions, the actual sum of the events and the value under the curve were compared for each fit. So eventual variations from the gaussian shape could be remaked, if the difference is to big. But in the case of the used data this was not the case, so the use of gaussian functions is justifiable. Another thing used for the verification of the results is the fitting error. If the fitting error was too high (in one single case higher than the actual value), the value was not used in the calculation of the ratio R. Two different fits can be seen in figure 3.1.

The value we get is the estimated value of the number of counts in the peak. This is calculated by subtracting the value of the area of the estimated background from the sum of the actual counts. So in the best case we have 5 valid values for each peak which we can compare once more. If there are some obvious deviations of one value from the other four, this value is also not used. Then the mean of the values and the standard deviation is calculated and afterwards the ratio R. For the ratio we also took the detector efficiency at the different ion energies into account: The ions are accelerated in a electric strong field, which is placed between a grid in front of the detector and the detectors front. This field is always at the same voltage of $V = 2550V$. With data from figure 3.2 (from [Kre+05]), we can determine the efficiencies for the single and double charged ion:

$$\eta^+ = 0.35 \pm 0.05 \ , \ \eta^{++} = 0.50 \pm 0.05 \ . \tag{3.3}$$

The error is just an reading error from the reading of the diagram. With this value one can calculate the ratio R:

$$R = \frac{n^{++}\eta^+}{n^+\eta^{++}} \ . \tag{3.4}$$

The results are shown in figure 3.3 (blue points).

Evaluation
The ratio $R = \sigma^{++}/\sigma^+$ can be seen in figure 3.3. To set this result in a context one can look at the data of [Sin+16]. This data is shown in figure
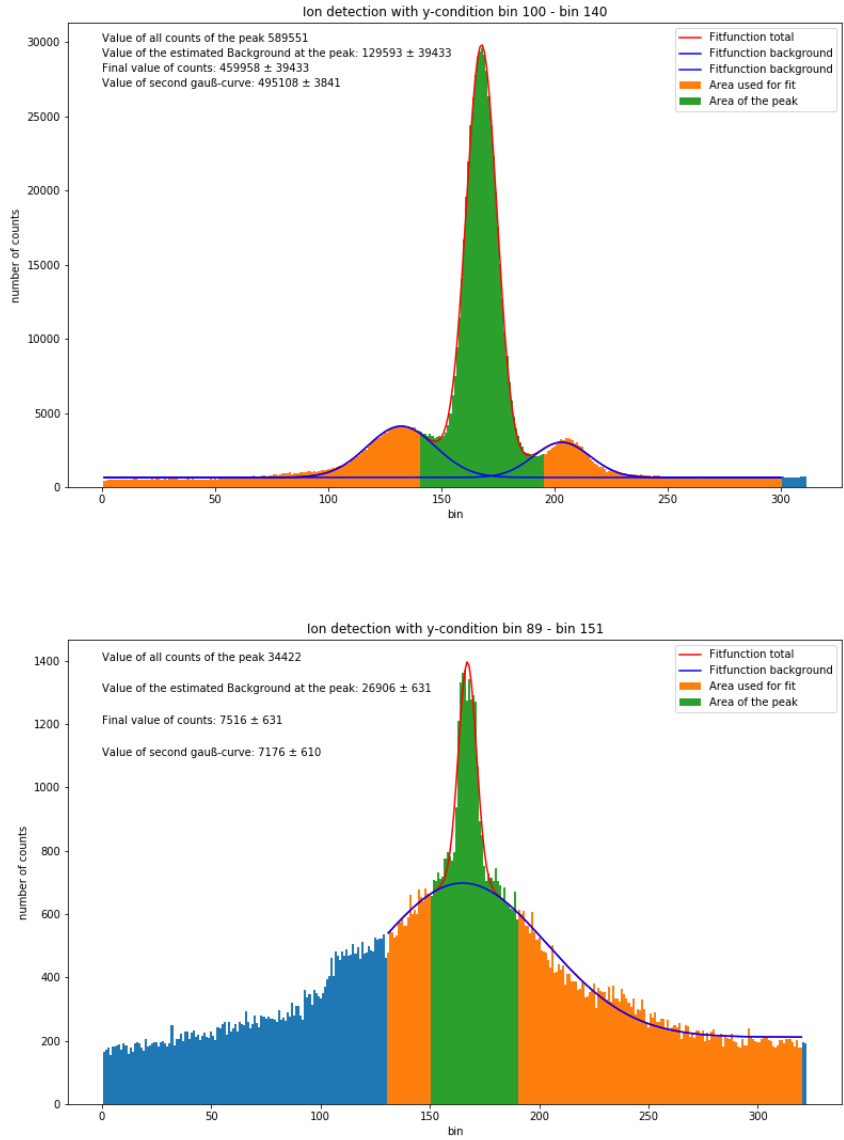
Figure 3.1: Evaluation in python: Upper side the Bz^+ and lower side the Bz^{2+} peak with a reduction of the y-range at an electron energy of $E = 41eV$.
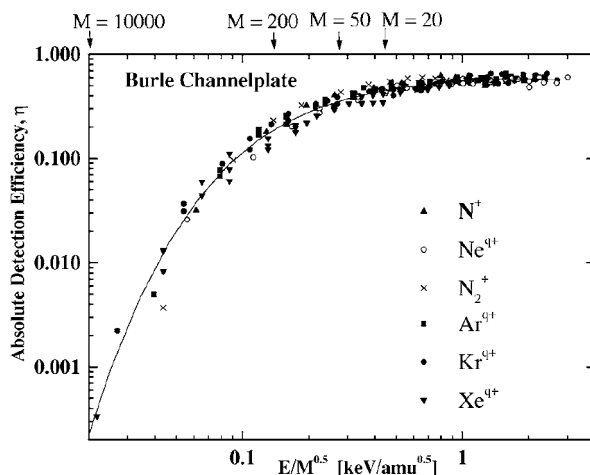
Figure 3.2: Detector efficiencies for a MCP detector in dependence of the ion energy and mass (from [Kre+05]).

3.4. We can see a peak of the single ionization cross-section at an electron energy of $\approx 60 - 80 eV$. From that we can estimate the approximate shape of the curve of the double ionization cross-section: It should be in general lower by several orders of magnitude and it should also have a peak, slightly shifted towards higher energies. This is due to the higher ionization energy and the lower probability of such an event. To investigate this behavior, the double ionization cross-section was calculated in the following way:

$$\sigma^{++} = R \cdot \sigma^{+} \, . \tag{3.5}$$

The value for σ^{+} was taken from the dashed line of figure 3.4. The results can be seen in the blue points of figure 3.5. This graph shows good agreement with our expectations: The absolute values of σ^{++} are by two orders of magnitude lower than the ones for σ^{+}. It is also visible that there has to be at least one peak between $41eV$ and $151eV$. The problem is the lack of more data: since we have only four data sets taken, this peak can not be further localized. So for a better evaluation, we would have to split the energy range up into smaller steps. This is what we later did in measurement 3.2. What also can be done is to take the data with the same measuring time and the same electron rate: If one would do that, one can directly compare the shape of the number of counts of the main peak dependent on the electron energy to
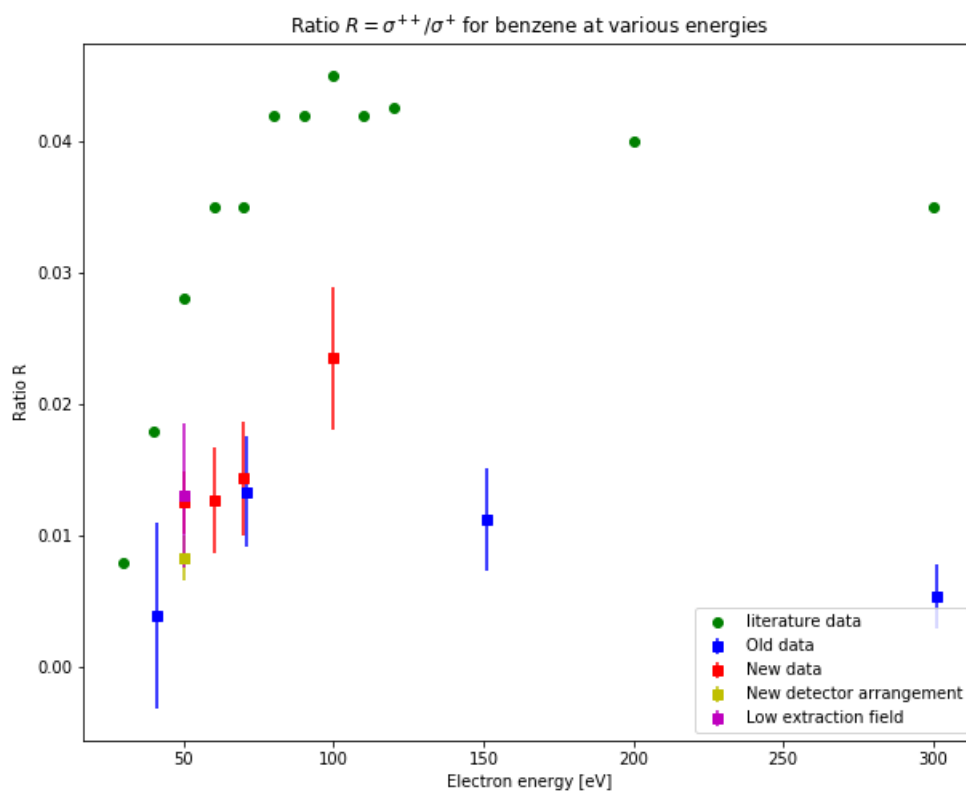
Figure 3.3: Ratio of the cross-sections $R = \sigma^{++}/\sigma^{+}$ for the single and double ionization of benzene at various energies. The literature data is from [Wol+20].
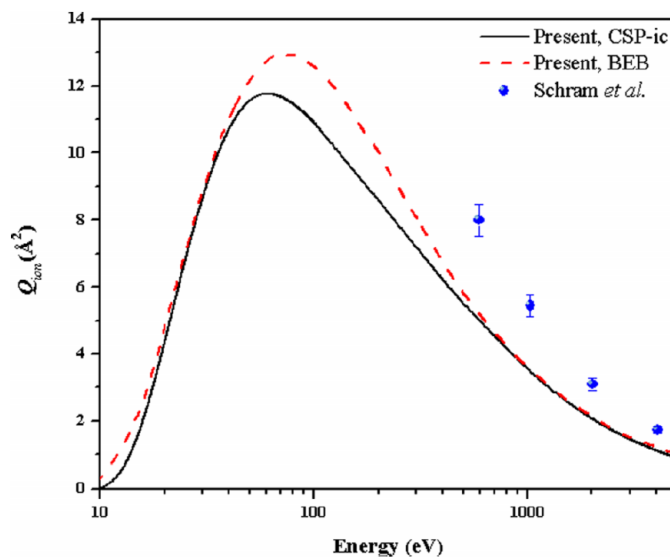
Figure 3.4: Single ionization cross-section for Bz, dependent on electron energy (from [Sin+16]).

the shape of the cross-section in figure 3.4. Since the counting rate is directly proportional to the cross-section and all the other variables are constant, on should see an identical shape.

Another thing we can do with this data is to compare it to the total ionization cross-section of benzene. One data set for this TICS is given in [Kim+04]. So from the values of figure 3.5 and figure 3.4, we can estimate the TICS:

$$\sigma_I = \sigma^+ + \sigma^{++} + \sigma_{ho} = (1 + R)\sigma^+ + \sigma_{op} \, , \tag{3.6}$$

where σ_{op} is the cross section for other ionization processes. Those processes are higher order ionization and dissociative ionization, where the latter one is the dominating part. So if we calculate $\sigma^+ + \sigma^{++}$, we can get an estimate of the contribution of σ_{op}. What one can see from figure 3.6, where the blue points are calculated from the measured data is, that the contribution of other processes is clearly visible.

One last thing to do is the estimation of the velocity of the supersonic gas-jet. So our model is that the velocity of the gas particles is exactly in the direction of the gas-jet. We also assume that the reaction volume is in the centre of the reaction chamber. So if an ion would be produced without any
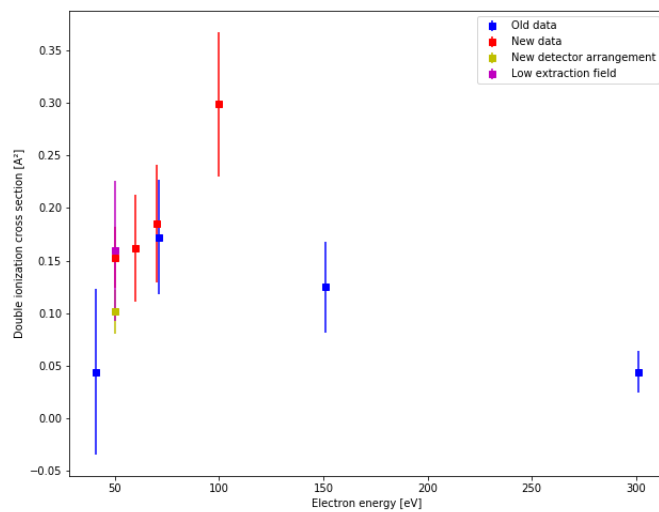
Figure 3.5: Calculated double ionization cross-section σ^{++} of benzene.
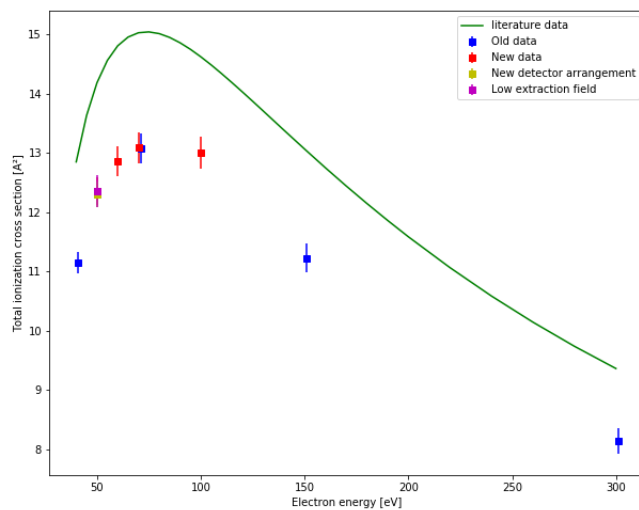

Figure 3.6: Calculated ionization cross-section $\sigma^{+} + \sigma^{++}$ for benzene and data for the TICS from [Kim+04].

momentum, it would hit the ion detector directly in the centre. Another thing to assume is that the momentum-transfer is symmetrical in x- and y-direction of the detector, so the centre of a peak is the position of an ion without any momentum transfer. With that assumptions, one can see that the y-position of the peak only depends on the jet-velocity:

$$y = v_{jet} \cdot TOF \,. \tag{3.7}$$

So if we use values from the fits of chapter 3.1, we can calculate the jet velocity:

$$v_{jet} = 1006\frac{m}{s} \,. \tag{3.8}$$

We can of course compare this value to some theoretical values: We can calculate the local sound velocities for the carrier gas helium and for the actual benzene (see chapter 2.2).

$$v_{He} = 1766\frac{m}{s} \tag{3.9}$$

$$v_{Bz} = 400\frac{m}{s} \tag{3.10}$$

So the velocity is clearly higher than the calculated value for benzene. This can be explained with the carrier gas helium: The velocity for helium is much higher, so the comparatively small amount of benzene is accelerated by collisions with the helium. After passing the nozzle, the gas is so thin that there are no collisions any more and the velocity remains lower than the theoretical velocity of helium. Also the estimation that the thermal energy is totally converted in kinematic energy is very simple, so the actual value for the velocity should be smaller.

One major problem in this measurement was the estimation of the backgrounds of the various peaks. This was, as mentioned previously, done with the relatively simple model of multiple Gaussian functions. Of course this is not the most accurate way to do this. But with respect to the amount of data, which has to be evaluated (10 sets of data for each energy), this is an efficient way to evaluate the data. Due to the differences between the data with respect to the different conditions used, one would also imagine that eventual errors would compensated by the other data. Another problem is, that the errors from the data is just the statistical error: For each point the mean of the values from different conditions was taken and the ratio was

calculated. The only error taken into account is the standard division of the means. But there are of course also some systematical errors: For example the error of a probably insufficient mathematical model can not be quantified that easy. Another problem is the estimation of the detector efficiency: We assumed it to be like the one of the detector in [Kre+05], but since we have a different model, it could differ from that.

3.2 New measurement on double ionization of benzene

As soon as there was some measuring time available on the experiment, we tried to first reproduce the data of the previous measurements and then make some additional measurements at different energies to further local-ize the peak of the double ionization cross-section σ^{++}. Therefore the first energy measured was $E_e = 70eV$. Then also measurements were done for $E_e = 50eV, 60eV, 100eV$. All measurements ran for 5-6 hours, so there is enough data to get a good statistical overview. In advance of each measure-ment, the electrostatic lenses and the magnetic field were optimized for a low background. Since those parameters only affect the direction of the electron beam, this has no effect on the good data.

Data analysis
The data analysis was done like previously (see section 3.1). All general settings for the $go4$ analysis were like in table 3.1. Also we evaluated each data set with the five different conditions.
One problem that occurred was that there was a short circuit in one of the delayline layers. Due to this, there were only two layers that produced posi-tional information. So as discussed in section 2.4.2, not as much missing data could be reconstructed. That effected dramatically the positional detection efficiency: The overall counts of the TOF-diagram were in the most cases twice as high as the overall counts in the x-y-diagram, while it would be equal if all counts had good position data. Therefore only the value from the fit directly out of the TOF-diagram was used in the calculation of the ratio R, together with the previously used correction. The other four evaluations were only used to check the shapes of the peaks. Because of this the error of each value is only the propagation of the fitting errors and the reading error

of the efficiencies.

Evaluation
Since the aim of this measurement was to reproduce the previous measurement, an electron energy of $70eV$ was used to compare the result with the previous measurement at $71eV$. What we can see from figure 3.3 is an excellent agreement within the errors (New measurements are the red points).
After this, for simplicity the electron energy was turned down by steps of $10eV$, since it is more easy to find the correct settings for the lenses and the magnetic field. So we measured two additional points at $60eV$ and $50eV$. Those points matched the estimated shape of the curve very well. Also one point at $100eV$ was measured because another experimenter had an measurement at this energy, so the settings were optimal and we used it to get another point with very low effort.
At the same time this measurement was done, the paper [Wol+20] was published. With this paper, there was the opportunity for a direct comparison of the values of the ratio R for the first time. The data can be seen in figure 3.3 (green curve). What can be seen is, that the shape of the curve and the location of the peak match very well. But the problem are the actual values: Our measured values are systematically too low by factor two. Since this paper is the first publication on that ratio, we had to verify our results separately in a different way.

3.3   Reference measurement with Argon

After this new measurement with the benzene it became clear that the ratio R is systematically lower than the published data from [Wol+20]. All the data is too small by a factor of two. To verify whether this is our fault, we made a measurement with the more common argon: For argon there are several established publications on the cross sections for single and double ionization (i.g. [JKR06] and [MSG92]).
The measurement was done at an electron impact energy of 150eV, simply because the experiment was set in an optimal way for this energy due to an experiment which ran in the meantime. Since the counting rate was relatively high and the measuring time was about 5-6 hours, the data set contains a more than sufficient amount of valid counts.
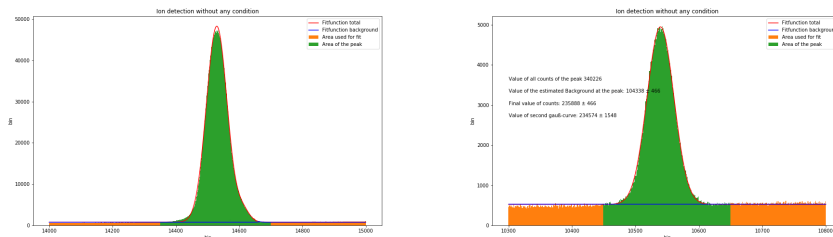
Figure 3.7: Evaluation in python: left side the Ar^+ and right side the Ar^{2+} peak directly out of the TOF-spectrum at an electron energy of $E = 150eV$.

Data analysis

The evaluation was done like in chapter 3.1, but also with the restriction of chapter 3.2, because the third delayline layer was still not working. As it can be seen in figure 3.7, the fit was much more easy in the case of argon. Since there are no fragments, the double ionization peak can be fitted with a single Gaussian function on a constant background. The single ionization peak is more or less the same, but we decided to use a second Gaussian for the breakup fragments of the dimer, which have, due to the breakup, a slightly longer TOF.

Evaluation

Since the mass of argon is significantly different from the one of benzene, new detector efficiencies are determined from figure 3.2 (from [Kre+05]). The new efficiencies are:

$$\eta^+ = 0.41 \pm 0.02 \, , \, \eta^{++} = 0.55 \pm 0.02 \, . \tag{3.11}$$

With that, the value of the ratio R could be calculated the same way as in chapter 3.1:

$$R(Ar) = (4.50 \pm 0.33)\% \, . \tag{3.12}$$

The error is once more just the propagation of the fitting errors and the reading errors. We can now compare this value to the published data: From the paper [MSG92] we have a value which was also taken in a crossed beam electron impact ionization experiment:

$$R(Ar)_{exp} = 8.31\% \, . \tag{3.13}$$

From the paper [JKR06] we have a value which is based on theoretical calculations:

$$R(Ar)_{theo} = 9.21\% \, . \tag{3.14}$$

One can see a good match of both values from the paper, but our result is once more smaller by factor two. This was the proof that our previous measurements were wrong and we had to improve the experimental setup for correct results.

One thing which could be thought of was the MCP. Since this MCP was in use for several years on electron-impact ionization studies in the same configurations, there are areas where the peaks were and other areas, where primarily just any background ions were detected. It is known that MCPs lose their efficiencies after a long time at high counting rates [Kre+05], and this is what happened locally on our detector. So what we see is a "efficiency hole" on our detector (see figure 3.8). It probably could happen that the peaks of the measurements are at the border of this efficiency hole, and therefore the double charged ions are detected with a slightly lower efficiency than the single charged ions.

Since the ions are always located on the same place on the detector, we can rotate the detector, so the ions would impact on a previously unused area of the MCP.

3.4   New detector setup

We decided to turn the detector by 180° for the next measurements. Therefore we had to bring the chamber to atmospheric pressure and disassemble the vacuum flange. Since dismounting the detector unit with the MCP and the delayline anode is very complicated (a picture of the unit can be seen in appendix A.2 and A.3), we decided to simply turn the whole unit by 180°. This can be easily done mounting the flange in the opposite direction. Of course this results in a upturned y-axis, but this is only relevant for any positional analysis, which is not necessary for the double ionization measurements.

After the detector was mounted, the vacuum was restored in the chamber and a test measurement was done with benzene. This measurement was done relatively quick, so there is not as much data as before, but since the aim of this measurement was to indicate any changes, this was sufficient. The
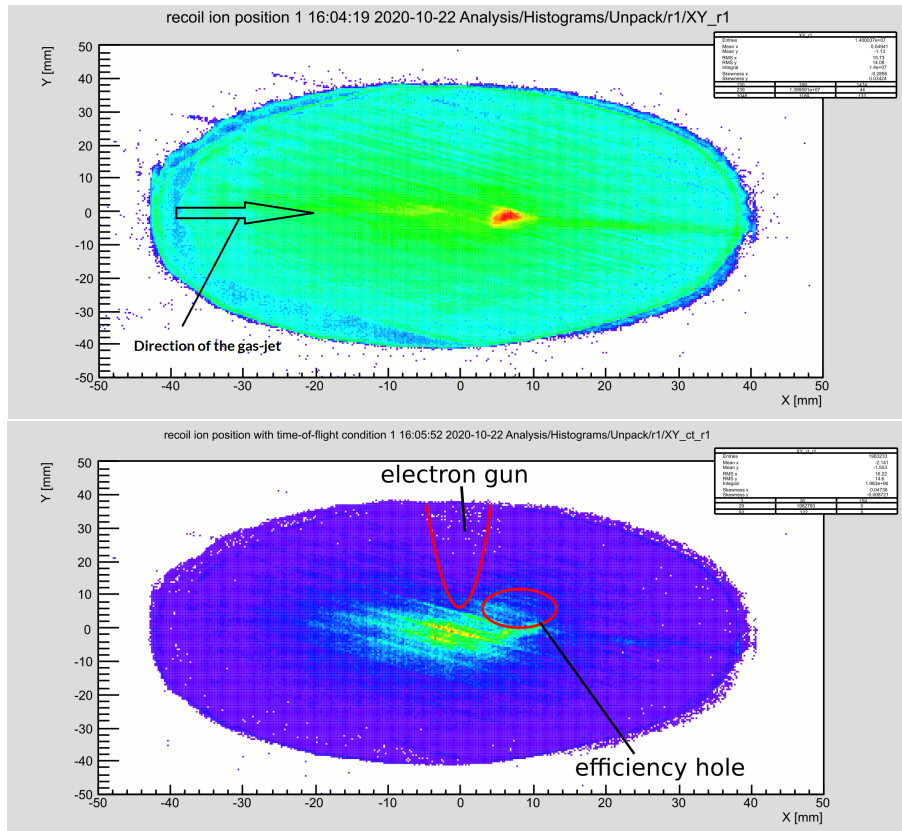
Figure 3.8: Efficiency hole on the detector: first the main peak of argon, plotted in a logarithmic scale for better visibility of other structures. In the second picture a TOF-region where no peaks are located is plotted. So there should be only background ions, for which we can estimate a symmetrical pattern. Therefore one can localize the efficiency hole and the shadow of the electron gun.

electron energy was $50eV$ because it was easy to restore the optimal settings and the signal to noise ratio was quite good at this energy.

Data analysis
The data analysis was done like before. Since we could not locate the error of the third delayline even with the dismounted detector, still only two layers were working. So the actual value is just calculated with the direct TOF analysis and the detector efficiencies from chapter 3.1. The errors are just as before only the fitting and reading errors. The result of this measurement was:

$$R = 0.83 \pm 0.17\% \tag{3.15}$$

Evaluation
The result of this new measurement can also be seen in figure 3.3 (yellow point). Surprisingly this value matches the expected curve of all measurements even better than the last measurement with an impact energy of $50eV$. Of course this is not good, because then the ratio is approximately the same as before. The small error is due to the nice shape of the peaks: The fit was very accurate, so the relative fitting error is smaller.

As a conclusion we can say that turning the detector did not improve the results of the measurement and we have to look for additional error sources. Of course the turn of the detector was nevertheless not disadvantageous. Since we now have a spatial homogeneous detection efficiency on the MCP, we do not have to think about that in the future.

Another effect that can be seen in figure 3.8 is the shading of the electron gun. To further investigate this, we evaluated a TOF-area, where no peaks, only background ions are located. Then we sliced out a small strip on the middle of the detector to see the effect of shading of the electron gun. The results of this evaluation can be seen in figure 3.9. What can be seen is that the shadow of the electron gun strongly effects the counting rate in the region between -6mm and +8mm. This is very problematic, since the double-ionization peaks of the different measurements are very close to this region. So a not negligible amount of ions are captured by the electron gun and are not detected, which lead to the small ratio of double ionized ions. So in order to measure the correct ratio, we had to get the double-ionization peak away from the shadow of the electron gun. This can be done by decreasing the
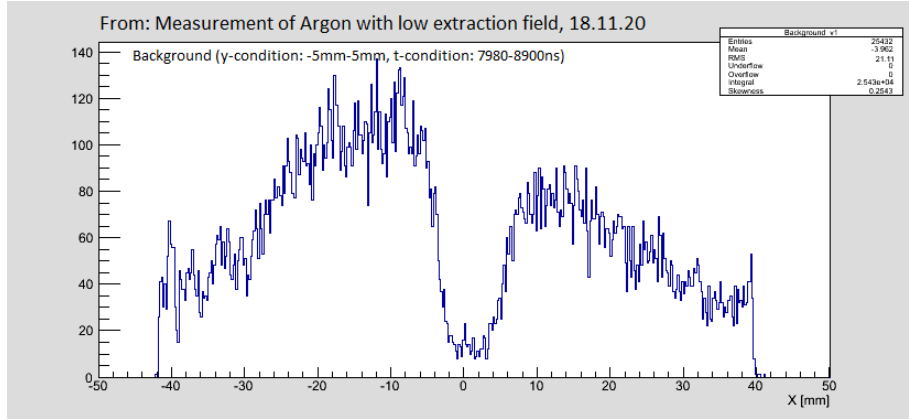
Figure 3.9: Shading of the electron gun on the ion detector

extraction field, what leads to a longer TOF. Since the vertical velocity of the ions is the target beam velocity, which is not affected, the longer TOF leads to a longer distance traveled in vertical direction.

3.5   Low extraction fields

We now tried to decrease the extraction field, so the strength of the field was chosen so that the single ionization peak of the benzene had a time of flight of approximately $17000ns$ (compared to $14000ns$ in previous measurements). The electron energy was once more $50eV$ since the experiment was set up for this energy and we could easily compare the result to the previous measurement. In addition, another measurement on argon was done with an electron energy of $100eV$. Again a low field was applied, so the TOF of the single ionization peak was at $20000ns$.

Data analysis
The data analysis was done like it is described in chapter 3.4. The results of this measurements were:

$$R_{lef}(Bz) = 1.31 \pm 0.54\% \,, \tag{3.16}$$

$$R_{lef}(Ar) = 5.13 \pm 0.47\% \,. \tag{3.17}$$

Evaluation

The result of the benzene measurement can also be seen in figure 3.3 (magenta point). It is a clear improvement compared to the previous measurement (yellow point). But it is somehow unclear why the result of the "new data" measurement (red point) is that close to the newest result. Since the TOF of the ions are more or less equal for the first three measurements, this result of the "new data" measurement at $50eV$ is probably incorrect.

Once more we can compare the measured value for the ratio of argon to the published data of [MSG92] and [JKR06]:

$$R(Ar)_{exp} = 8.3\% \, , \tag{3.18}$$

$$R(Ar)_{theo} = 9.3\% \, . \tag{3.19}$$

Compared to the result of chapter 3.3, where the published ratios were almost the same, but the measured value was smaller than in this measurement, one can see a small but noticeable improvement. The problem is now, that we cannot increase the TOF any further that easily because of the experimental framework: Every $25\mu s$ (with a small uncertainty), the laser produces one pulse. Therefore the data acquisition is set up in a way that it is triggered by the laser pulse and opens a detection window of $20\mu s$. One way to extend the possible TOF-range is to delay the triggering signal from the laser. Then one can shift the detection window to longer TOF. Of course one would then see some short-TOF ions from the next pulse, but since those ions are normally only background ions, one can consider that in the data evaluation.

3.6 New experimental setup

Even if we had some promising results in the measurements we did in chapter 3.5, we decided to switch to a new experimental setup, which is described in chapter 2.6. With this setup we tried to first measure the single- to double-ionization curve of argon and then of benzene.
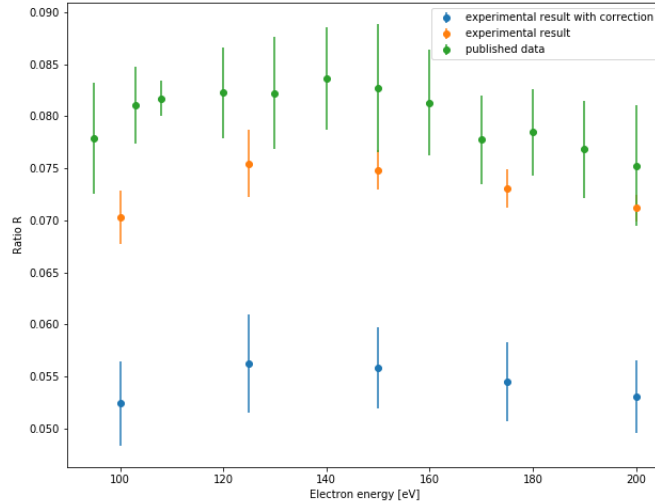
Data analysis

Figure 3.10: Measured Ratio R for argon in the new experimental setup and published data from [MSG92].

In this experiment, the *go4* software is not used. Instead, there is a more simplified software called *CoboldPC*. In this software, it is also possible to apply some conditions on the data. For example in the argon measurement, there was a x- and y-condition applied simultaneously to reduce the background. This was necessary because the double ionization TOF-peak was located in an area where lots of background occurred. In x- and y-direction, this background can be clearly separated from the *Ar*-ions, so this conditions worked properly. For the measurement with benzene, this was not necessary. The determination of the valid counts was done with the *python*-routine similarly as before.

Evaluation

The measurement on argon gave much better results than before (see figure 3.10). The uncorrected results matches the published data within the errorbars. So we see that the correction with the data of [Kre+05] does not help in this case. This is probably due to the other MCP-model used in our experiment. So we do not use this correction in the following measurements.
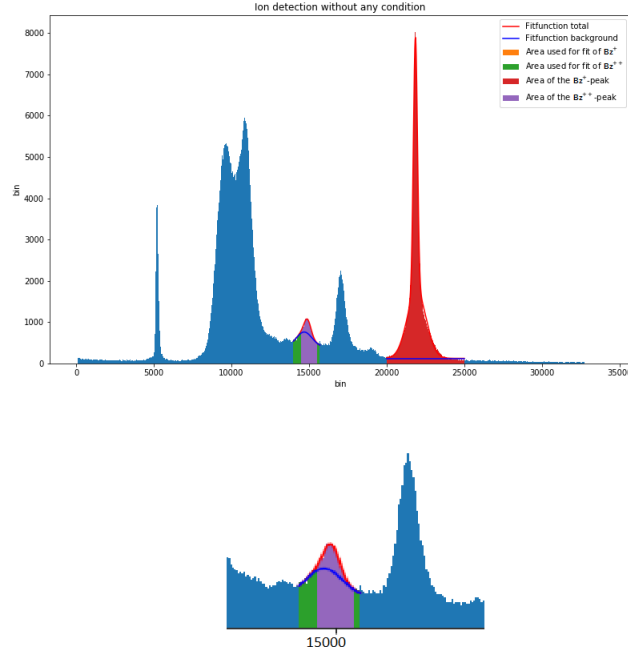
Figure 3.11: Spectrum of benzene at $E_e = 175eV$. On can see the merging peaks and the uncertainty of determining the background, especially at the Bz^{++} peak. An enlargement of this is shown in the lower picture.

One can see that the shape of the curves are very similar and the position of the global maximum is more or less the same, if one notes our curve has much less measuring points. There seems to be a systematic offset towards lower values. This is probably due to the characteristics of this MCP.

However these results did stir up expectations on the measurement with the benzene. But we were disappointed: The TOF-resolution of this new experimental setup is not as good as before. Therefore, the $C_6H_6^{++}$ peak was not distinguishable from the $C_3H_3^+$ peak. Another result of this lower resolution is, that the $C_6H_6^+$ and the $C_6H_5^+$ peaks merges (see figure 3.11). Because of this, the actual numbers of counts can not be determined accurately and no ratios could be calculated.

The lower resolution is the result of various factors: In the new setup, a high voltage pulse generator is used to generate the spectrometer voltage. This

generator creates pulses out of a constant current, which also sets the voltage of the pulses. This constant current is made by a laboratory power supply, which is not really stable. Therefore, the pulses get broadened because of the different TOF of the equal ions due to the unstable spectrometer voltage. Another problem is, that the spectrometer voltage is delayed and ramped up. This leads to a inhomogeneity in the field, and the ions do not have equal time of flights. Another thing on this experiment is the spectrometer geometry: In the normal case, the drift tube between the spectrometer and the detector is twice as long as the actual spectrometer. This leads to the so called $time - focusing$, where the TOF is independent of small deviations in the reaction area (For a detailed description see chapter 2.4 in [Fis00]). This special geometry is not exactly used in this experiment, so the time-focusing does not work properly.

So what we did in a second run with benzene was to replace the laboratory power supply against a digital power supply, which was more stable. We also tried to apply a timely constant field and it worked just fine at higher energies, but we had to deflect the electron beam in the opposite direction, which was no problem due to deflectors in the electron gun. For lower electron energies ($E_e < 150eV$), this did not work, since the electrons are to slow and get deflected to much by the spectrometer. Therefore, the peak broadened more and more. So for the low energies, we used the pulsed spectrometer voltage, but with higher absolute voltage values to reduce the time of flight. With this changes, we got excellent TOF resolution in this experiment. The result can be seen in figure 3.12.
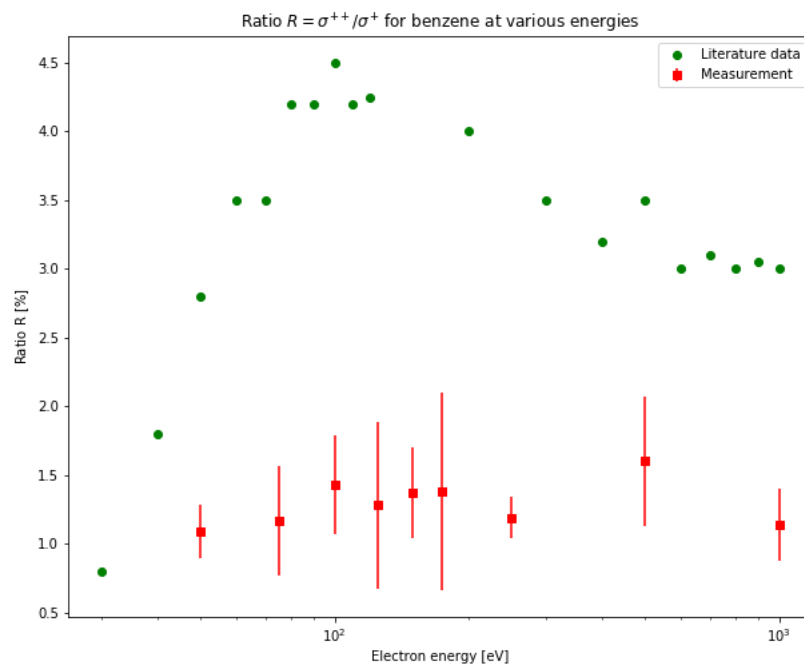
Figure 3.12: Final measurement of the ratio R of benzene with the improved new experimental setup. For comparison, the literature data from [Wol+20] is plotted.

Chapter 4

Discussion, summary and outlook

In this chapter, a further discussion on the experimental results is given and especially the measured ratio R is explained in detail. In the end, a small summary on all the measurements is given and an outlook on further interesting research fields is given.

4.1 Discussion of the measurement of the ratio R

We have measured the ratio R between the single and double ionization cross section for argon and benzene in a wide range of energies. Therefore we can discuss this curves 3.12 and 3.10 with respect to different energy ranges.

High energy limit
For high projectile energies, which correspond to high projectile velocities, on the theoretical point of view only the first Born approximation should count for the ionization. As described in chapter 1.3.1, this corresponds to a single interaction of the projectile and the target. In our measurements, the ratio R for high energies is non-zero. So we have other processes in our molecules and atoms. One possible process is the TS1 process, another process is the SO-mechanism (see chapter 1.2.2). In both processes, the electron-correlation in the molecule or atom plays an important role. Since in big atoms or molecules (like benzene and argon) the electrons do have a lower binding en-

ergy, those correlations between the electrons are way stronger than in small atoms (like helium), the double ionization cross section is higher at bigger energies. This can be also be seen if one compares our data to the one from [Sha+88], where the ionization of helium in electron-atom-collisions is measured. For electron energies of $E_e = 200eV$ and $E_e = 1000eV$ there are the ratios $R_{He}(200eV) = 0.5\%$ and $R_{He}(1000eV) = 0.47\%$. As expected, this ratios are smaller than our measured values. Especially the argon value is much higher, even higher than the one for benzene. This is because of the atomic structure of the argon. Here an electron from an inner shell can be removed, triggering an outer shell electron to fall down in the inner shell. The released energy is then used to remove a second electron. This is the so called auger decay, which can not happen in a benzene molecule, because, as we have seen in chapter 1.4, the benzene molecule dissociates when a inner shell electron is removed.

Moderate energies
Coming from high energies, we see an increase of the ratio towards lower energies in both measurements, the one from argon and benzene. This is the contribution of the second Born approximation. Here we see processes where the projectile electron interacts with the target twice. This is now possible due to the lower velocity of the projectile. Of course the previously discussed processes are still possible. One can once more see that the maximum ratios of benzene and argon are much higher than the one of helium, which is for example $R = 0.55\%$ ([Sha+88]). This is due to the previously discussed properties of bigger atoms and molecules.

Low energy limit
If one sets the projectile energy at lower values, the ratio goes down again. This is due to the approach on the double ionization threshold. If the projectile energy is only a little above this threshold, there is only a small amount of possible momentum configurations, since the recoil ion and the three electrons momentum is very small. So in some configurations the released electrons would be caught again by the ion. Therefore the double ionization cross section decreases and is zero at the double ionization threshold. This also explains the different falling of the ratio of helium, argon and benzene. Since their double ionization thresholds are $E_{He} = 54.42eV$, $E_{Ar} = 27.63eV$ and $E_{Bz} = 25.6eV$, the behavior of argon and benzene are very similar at these low energies, while the ratio of helium is going down at higher energies.

4.2   Summary and outlook

In this work, a quantitative measurement of relative yields for ions of different charge to mass ratios was done for the first time on the firstly used reaction microscope. Previously, there were only studies where the reaction products are evaluated for their momentum and type or measurements on co-incidences (i.e. [Ren+14], [Ren+18]). So the experimental work which is now done showed the problems of this kind reaction microscopes for quantitative measurements. The recorded data gives a good overview on the problematic zones of the ion detector. The efficiency hole was brought to the opposite side of the ion impact zone, so this should not effect any measurements in the future. Also the shadow of the electron gun was quantified (see figure 3.9). So this can help to find problems more easily in future experiments. A strategy for optimization of the quantitative results was developed, which included the extension of the TOF of the ions even above the laser pulse-repetition-time of $25\mu s$. Unfortunately, this could not be tested in the experiment due to the switching to another experimental setup.

For this reason, the experimental results gained on this reaction microscope do not match the literature data. In qualitative consideration, one can see a accurate accordance of the measured data shape and the literature curve of the ratio R (see figure 3.3). Also the position of the measured maximal ratio agrees to the literature data. What also can be seen in the experiments is the dissociative ionization of the benzene (see figure 1.4), but this was not further investigated. This would be an interesting field for future research, since there is literature data for the fragmentation of benzene in photoionization processes ([Tal+00] and [Hol+02]), so one could compare the behavior in electron-impact-ionization processes.

On the second experimental setup, the ratio R of argon could be reproduced quite accurately compared to the literature data (see figure 3.10). This is due to the lack of an electron gun in front of the detector. So now all ions which fly in the direction of the detector can in principle be detected. Of course one also has the disadvantage of the limited detector efficiency here. For the measurement of benzene, we applied a constant spectrometer voltage and improved the spectrometer resolution with that. This can also help in further research on this experimental setup, because one not not only has the better resolution, but also has a wider TOF-area accessible because the short TOFs are not affected by the ramping of the voltage any more.

What is still somehow unclear are the absolute values of the ratio in the

benzene measurement. Those are still much lower than the published data from [Wol+20]. It is quite problematic that there is no error data in this publication. So we do not have any idea how accurate their measurement is. Another problem with these measurements done in the literature data is that the ions are detected in a reflectron mass spectrometer, so they fly over a longer distance and are even reflected by an electrical field. Also the time of flight focusing does not work. So in principle this can cause errors which could lead to a higher detection efficiency for doubly ionized molecules. Our lower values also can not be explained by the characteristics of the MCP: In general, the double ionized ions have higher kinetic energy and therefore higher detection efficiencies. So this would normally lead to an underestimation of the singly charged ions and therefore to an overestimation of the ratio R. As a conclusion we can say that we can not explain this result at the moment and that we have eliminated all of the probable error sources in the experimental set ups that came to our mind. So this could be worth another measurement in a different kind of experimental setup to prove whether our results or the results of [Wol+20] are correct.

So this is a good example to show how up-to-date these kind of measurements are. For rare gases, there is a good amount of data on the electron-induced ionization (e.g. [MSG92],[Sha+88]), but for more complex molecules like benzene or other organic building blocks the research is still going on.

Bibliography

[AKi+88]   A.Kiermeier et al. "Multiphoton Mass Spectrometry of Clusters: Dissociation Kinetics of Benzene Cluster Ions". In: *J. Phys. Chem.* 92 (1988), p. 3785.

[Bor26]   Max Born. "Die Quantenmechanik der Stoßvorgänge". In: *Zeitschrift für Physik* 37 (1926), pp. 863–867.

[Dem16]   A. J. Dempster. "The ionization and dissociation of hydrogen molecules and the formation of H 3". In: *The London, Edinbourgh and Dublin Philosophical Magazine and Journal of Science* 31 (1916), p. 438.

[DRM88]   D.R.Miller. "Free jet sources". In: *Atomic and Molecular Beam Methods*. Oxford University Press, 1988.

[Dür06]   Martin Dürr. "Electron Induced Break-up of Helium: Benchmark Experiments on a Dynamical Four-Body Coulomb System". Dissertation. Combined Faculties for the Natural Sciences and for Mathematics of the Ruperto-Carola University of Heidelberg, Germany, 2006.

[Fis00]   Daniel Fischer. "Aufbau eines Reaktionsmikroskops zur Untersuchung von Ion-Atom-Stößen". Diplomarbeit. Fakultät für Physik, Albert-Ludwigs-Universität, Freiburg im Breisgau, 2000.

[HKE03]   Mathias Hillenkamp, Sharon Keinan, and Uzi Even. "Condensation limited cooling in supersonic expansions". In: *Journal of chemical physics* 118 (2003), p. 8699.

[Hol+02]   D.M.P. Holland et al. "A time-of-flight mass spectrometry study of the fragmentation of valence shell ionised benzene". In: *International Journal of Mass Spectrometry* 220 (2002), pp. 31–51.

[JKR06]   L.K. Jha, S. Kumar, and B.N. Roy. "Electron impact single and double ionization of argon". In: *The European Physical Journal D* 40 (2006).

[Jüsar]   t. Jüstel. *Austrittsarbeit (Work function table).* unknown year. URL: https://www.fh-muenster.de/ciw/downloads/personal/juestel/juestel/chemie/Austrittsarbeit.pdf.

[Kim+04]   Y.-K. Kim et al. *Electron-Impact Cross Sections for Ionization and Excitation Database.* 2004. URL: https://physics.nist.gov/cgi-bin/Ionization/table.pl?ionization=C6H6xx0.

[KN87]   O. Kitao and H. Nakatsuji. "Cluster expansion of the wave function. Valence and Rydberg excitations and ionizations of benzene". In: *The journal of chemical physics* 87 (1987), p. 1169.

[Kre+05]   M. Krems et al. "Channel electron multipliers and channelplate efficiencies for detecting positive ions". In: *Review of Scientific Instruments* 76 (2005), p. 093305.

[LKK16]   H.P. Latscha, U. Kazmaier, and H.A. Klein. *Organische Chemie. Chemie-Basiswissen II.* 2016. ISBN: 978-3-662-46179-2.

[MSG92]   P. McAllion, M. B. Shah, and H. E. Gilbody. "A crossed beam study of the multiple ionization of argon by electron impact". In: *Journal of Physics B: Atomic, Molecular and Optical Physics* 25 (1992), p. 1061.

[MW95]   Ian E. McCarthy and Erich Weigold. *Electro-atom collisions.* 1995. ISBN: 0 521 41359 1.

[Pfl]   Thomas Pflüger. *Versuchsanleitung F22 Stoßionisation von Atomen.*

[Pfl12]   Thomas Pflüger. "Electron Impact Ionization Studies of Small Rare Gas Clusters". Dissertation. Combined Faculties for the Natural Sciences and for Mathematics of the Ruperto-Carola University of Heidelberg, Germany, 2012.

[Ren+14]   Xueguang Ren et al. "An (e, 2e + ion) study of low-energy electronimpact ionization and fragmentation of tetrahydrofuran with high mass and energy resolutions". In: *Journal of chemical physics* 141 (2014), p. 134314.

[Ren+18]   Xueguang Ren et al. "Experimental evidence for ultrafast in-
           termolecular relaxation processes in hydrated biomolecules". In:
           Nature Physics 14 (2018), pp. 1062–1066.

[Sch+97]   H.T. Schmidt et al. "A design study for an internal gas-jet target
           for the heavy ion storage ring CRYRING". In: *Hyperfine Inter-
           actions* 108 (1997), p. 339.

[Sha+88]   M. B. Shah et al. "Single and double ionisation of helium by
           electron impact". In: *Journal of physics B: Atomic, Molecular
           and Optical Physics* 21 (1988), p. 2751.

[Sin+16]   Suvam Singh et al. "Calculation of total and ionization cross
           sections for electron scattering by primary benzene compounds".
           In: *The journal of chemical physics* 145 (2016), p. 034309.

[Tal+00]   A. Talebpour et al. "Dissociative ionization of benzene in intense
           ultra-fast laser pulses". In: *Journal of Physics B: Atomic, Molec-
           ular and Optical Physics* 33 (2000), pp. 4615–4626.

[Wan53]   Gregory H. Wannier. "The Threshold Laws for Single Ionization
           of Atoms and Ions by Electrons". In: *Physical reviev* 90 (1953),
           p. 817.

[Wiz79]   Joseph Ladislas Wiza. "Microchannel Plate Detectors". In: *Nu-
           clear Instruments and Methods* 162 (1979), p. 587.

[Wol+20]   Wania Wolff et al. "Production of Long-Lived Benzene Dications
           from Electron Impact in the 20-2000 eV Energy Range Combined
           with the Search for Global Minimum Structures". In: *The journal
           of physical chemistry A* 124 (2020), pp. 9261–9271.

Appendix A

Photos of the experimental set up

Figure A.1: Photo of the experimental set up. One can see the Helmholtz coils (Yellow isolation) and the square shaped coils to shade the earths magnetic field (In the metal profiles). In the middle of the coil arrangement, the vacuum chamber is located.
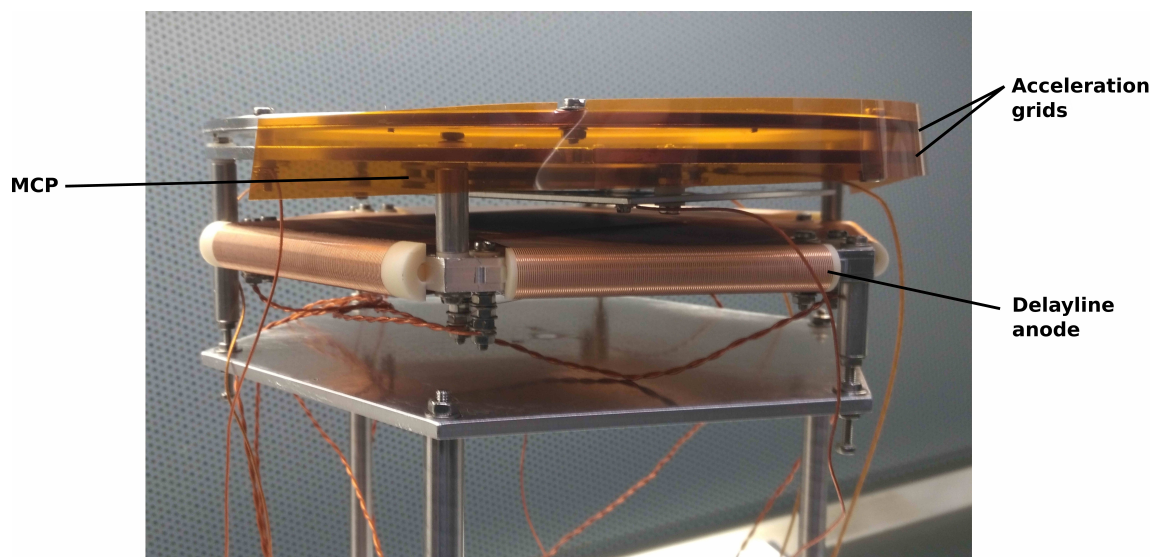
Figure A.2: Photo of the ion detector head. One can clearly see all components which are necessary for the position and time sensitive detection of ions.
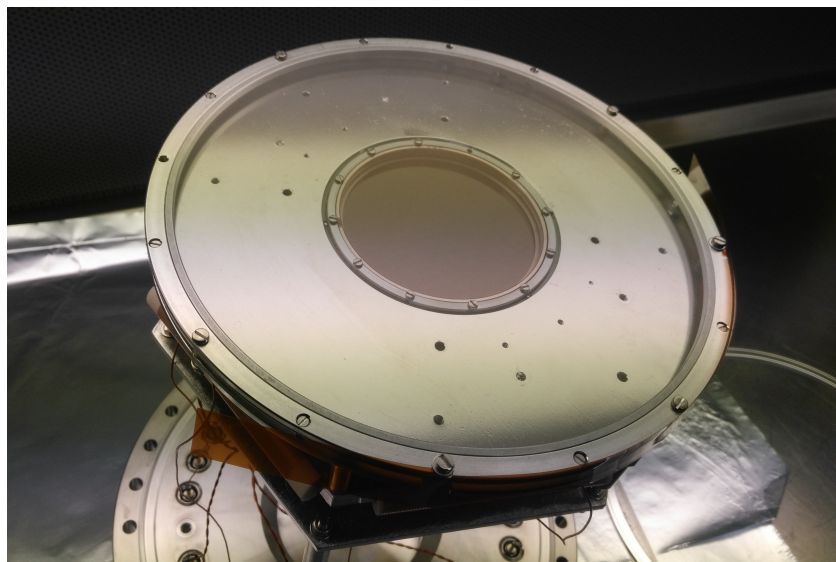

Figure A.3: Photo of the top of the ion detector, where the ions are coming in. One can see the acceleration grid on the top and the smaller MCP in the middle.
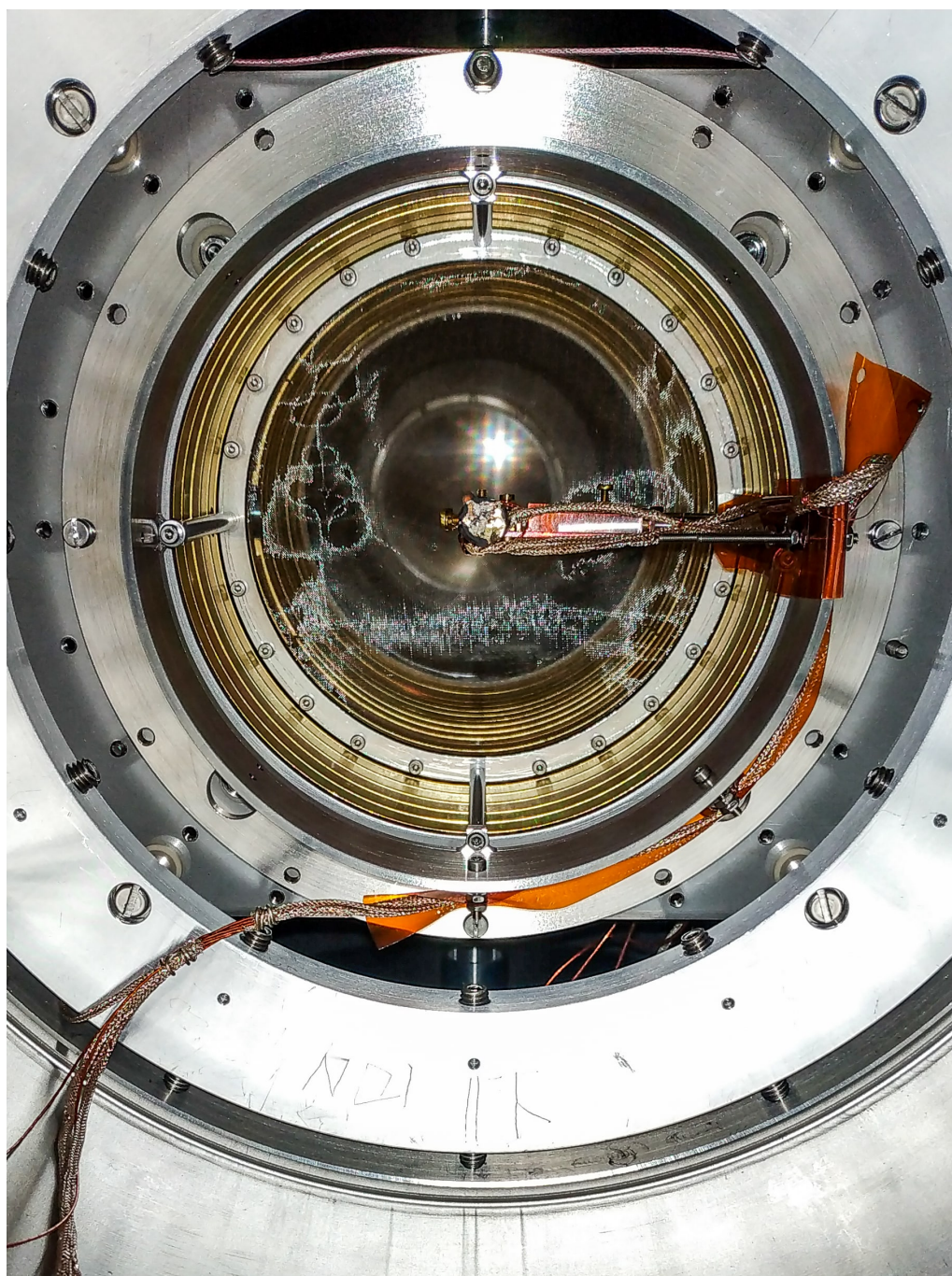
Figure A.4: Frontal view in the main chamber from the place of the ion-detector. One can see the electron gun, its electrical supply and the mechanical suspension. Behind it, there is a metallic grid, which stops the acceleration field. In the background one can see the MCP of the electron detector (Photo by A.Dorn).
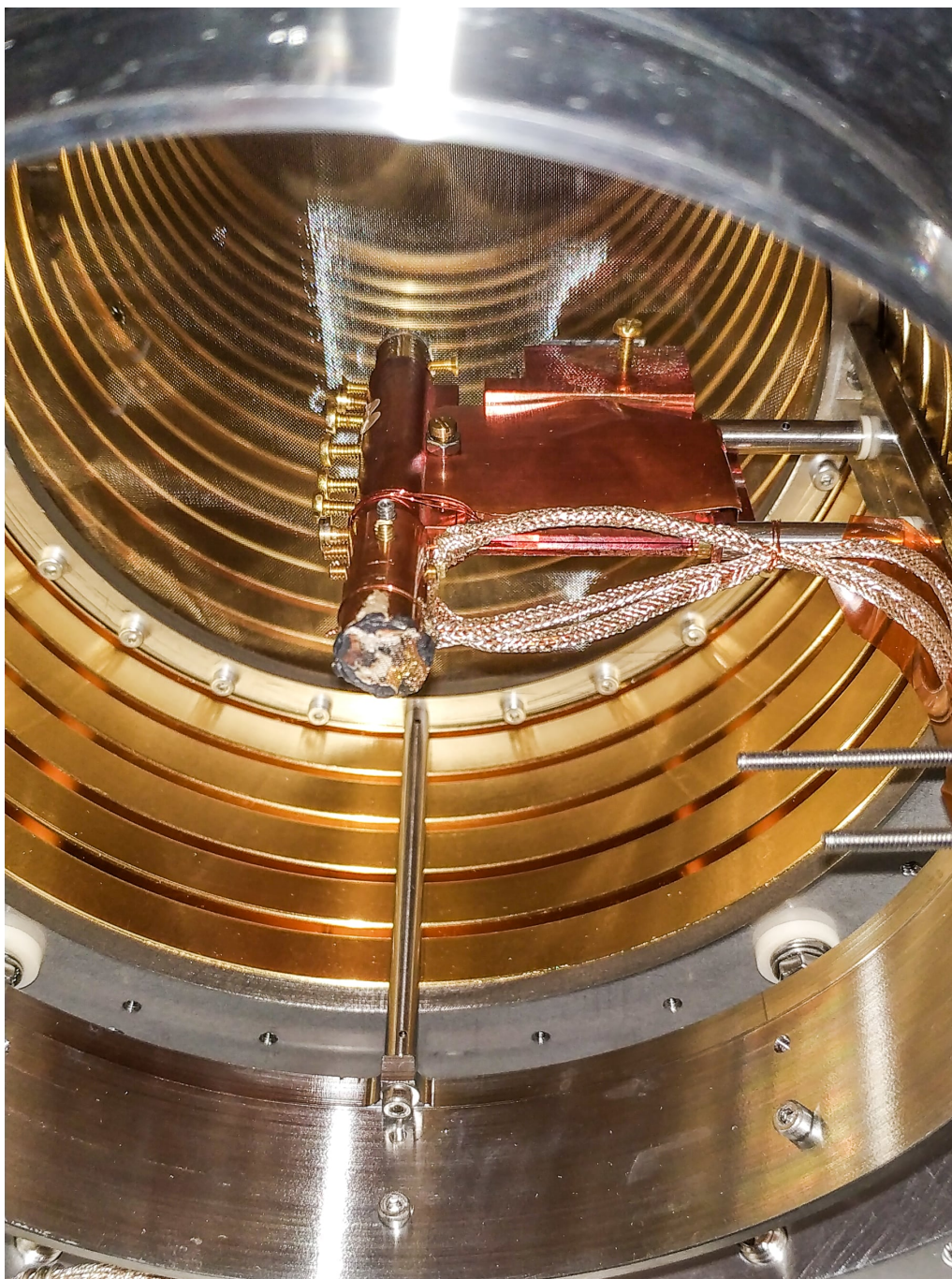
Figure A.5: Another view on the electron gun. One can now also see the spectrometer rings and once more the grid at the end of the spectrometer. The five rings in front of the grid are not in use any more (Photo by A.Dorn).

Erklärung

Ich versichere, dass ich diese Arbeit selbstständig verfasst und keine anderen als die angegebenen Quellen und Hilfsmittel benutzt habe.

Heidelberg, den 18.12.2020,